UNIVERSITY OF OKLAHOMA

GRADUATE COLLEGE

REVEALING CHANNELIZED FEATURES THROUGH MULTI-SCALE WORKFLOWS IN A MIXED CARBONATE SILICICLASTIC SETTING, GRAYBURG AND SAN ANDRES FORMATIONS, MIDLAND BASIN, TX.

A THESIS

SUBMITTED TO THE GRADUATE FACULTY

in partial fulfillment of the requirements for the

Degree of

MASTER OF SCIENCE

By

LAURA LUCIA ORTIZ SANGUINO

Norman, Oklahoma

2023

REVEALING CHANNELIZED FEATURES THROUGH MULTI-SCALE WORKFLOWS IN A MIXED CARBONATE SILICICLASTIC SETTING, GRAYBURG AND SAN ANDRES FORMATIONS, MIDLAND BASIN, TX.

A THESIS APPROVED FOR THE

SCHOOL OF GEOSCIENCES

BY THE COMMITTEE CONSISTING OF

Dr. Heather Bedle, Chair

Dr. Matthew Pranter

Dr. Sumit Verma

Acknowledgements

First of all, I would like to thank Fasken Oil and Ranch for the C-Ranch 3D 2019 seismic survey used in this research. To Schlumberger and Ellis for their kind donation of Petrel 2022 and Paleoscan 2022 used for seismic visualization and interpretation purposes. Also, thanks to the Attribute-Assisted Seismic Processing and Interpretation (AASPI) consortium for providing licenses for attribute analysis and funding, Emerson for the licenses of Geolog21 used during the petrophysical analysis and CGG for providing the Hampson Russell academic license used for the well-tie process. Thanks to Dr. Fnu Sumarin and Dr. Abidin Caf for their valuable input and guidance.

To my committee members Dr. Heather Bedle, Dr. Matthew Pranter, and Dr. Sumit Verma, for guiding me in every step of this project and encouraging me to never give up and see the bright side during the rough times. Special thanks to Dr. Bedle for believing in me and being my best cheerleader and coach! To all my friends Karelia La Marca, Bobby Buist, Emily Jackson, Diana Salazar, Ganiyat Shodunke, Raymond Ng, Mario Ballinas, Camila Castillo, Camilo Mateus, Javier Tellez, Marcus Maas, among many others for every piece of advice and support. I enormously appreciate every hug, talk, meal and/or sleepless night we shared.

To the Colombian Student Association, Mewbourne College and School of Geoscience staff for providing me scholarships and awards that helped me succeed in this journey. Also, for being a family and standing by my side when I needed aid. Special thanks to my fellow Colombians in COLSA, for bringing a piece of my country to OK and reminding me my roots.

To my family in Colombia Blanca, Enrique and David for being an unconditional support and the motivation to do everything I do. I feel the luckiest person in the world to call you my family and

I admire every effort you do for me. To my OK host family Gloria and Mitch Burrus and all the students' part of our beautiful family for brightening my days and cheering me up when I needed it the most. To the Silver family, for welcoming into your family and being there for me in the toughest (and happiest) moments.

To my life partner Brandon A. Silver for his endless emotional support and care. You are my rock and my inspiration. I can't wait to start our own tiny little family with our puppies (Timmy and Taco (TBD) Silver).

Lastly, to OU for giving me the greatest chapter of my life. Here I learned all about friendship, love, and academia, and can't thank you enough for all the lessons you taught me that are far beyond a classroom. I am infinitely grateful with God for bringing me all the way here, right where I belong. Now it is time for me to move on, not without leaving in this land a bit of my tropical soul.

TABLE OF CONTENTS

LIST OF TABLES

LIST OF FIGURES

Abstract

Channelized systems in mixed carbonate-siliciclastic settings are challenging to characterize from the geological standpoint as facies variability is expected to be high (e.g., siliciclastic porous channel fills, carbonate cemented channel fills or even carbonate channel fills). Determining the lithological composition is crucial for not only understanding the basin evolution but also is required for drilling plans either if the channels serve as reservoirs or drilling hazards.

An example of one such compositionally mixed channel system is identified in the San Andres and Grayburg formations in the Midland Basin, TX. For this specific example, channels are presumably siliciclastic infilled while the shelf the channels cut across is dominantly carbonate. An integrated study of core, well-log, and seismic data is conducted to analyze the facies variability of the channelized interval and understand its geomorphological evolution. Seismic attributes such as coherent energy, sweetness and spectral components (CWT) prove to be the most efficient at enhancing the contrast between the clastic vs carbonate elements; demonstrating that it is feasible to depict the lithological heterogeneity between the channel infills and the shelf at a seismic scale. Additionally, conventional seismic interpretation and geometric attributes (e.g., apparent dip, dip azimuth and magnitude, etc.) suggests two categories of channel incisions: type I, characterized by V-shaped bases, straight and mostly oriented in a NE-SW direction; and a type II, that tend to be U-shaped, slightly sinuous, and oriented in a NW-SE trend. Well-log based litho-density techniques such as ρmaa-Umaa and core descriptions support the seismic observations by illustrating the vertical and horizontal heterogeneity and how the channel infills are dominantly siliciclastic in nature. A 3D lithology model constrained to the previous analyses illustrates a dominance of siliciclastics in the Lower San Andres while the Upper San Andres and Grayburg are limestone-rich with episodic siliciclastic events (i.e., related to the channel incisions) and dolostone (in the Upper Grayburg). Lithologies and morphological changes are directly related to changes in the sea level and source rock composition. This study is pioneering in its understanding of the siliciclastic deposition in the middle Guadalupian units in this portion of the Midland Basin, which are referred in literature as the *Midland sands* and identified as analogs of the Brushy and Cherry Canyon formations in the Delaware Basin.

Keywords

Mixed carbonate-siliciclastic environments, seismic attributes, 3D modeling, Permian Basin, channel geomorphology.

Introduction

The Permian Basin, located in west Texas and southern New Mexico, accounts for approximately 43% of the oil and 17% of gas production in the United States (EIA, 2022). Mixed carbonate-siliciclastic deposition is common in this basin, specifically in the Grayburg and San Andres formations. These units have long been the backbone of conventional hydrocarbon reservoir production (Dutton et al., 2005a, b), with ongoing extraction through both waterflooding (Entzminger et al., 2000; Petersen & Jacobs, 2003) and tertiary recovery (Entzminger et al., 2000; Petersen & Jacobs, 2003; He et al., 2019). Due to the depositional and diagenetic complexity and lack of data quality (Verma et al., 2023; Yalcin et al., 2019) and limited integration (Lee et al., 2018; Yandel et al., 2019), these units are poorly understood in the Midland Basin. A detailed analysis of the geomorphological expression and the lithological changes is performed and integrated at different scales (core, well log, and high-quality seismic) to build a depositional history for the aforementioned intervals.

Mixed carbonate-siliciclastic geological settings are complex as extrabasinal (siliciclastics) and intrabasinal produced (carbonates) sediments are mingled as a result of complex interactions between fluviodeltaic discharge and currents in carbonate areas (Chiarella & Longhitano, 2012; Chiarella et al., 2017; Moscardelli et al., 2019). The mixture of siliciclastic and carbonate sediments can be observed as lateral facies mixing and/or temporal variability in the sediment type (episodic deposition of carbonate and siliciclastic related to sediment supply or stratigraphic occurrence) (Ortiz-Sanguino et al., 2022). Depositional episodes are normally driven, along with other factors, by sea-level fluctuations that are better understood within a sequence-stratigraphic framework. Lowstand system tracts (LST) are dominated by siliciclastic sediment while transgressive (TST) and highstand system tracts (HST) are characterized by carbonate deposits (Zonneveld et al., 2012; Garcia-Hidalgo et al., 2007). A depositional model that suits this setting is *build-cut-fill-spill*, which divides the deposition into four stages, and it is used to explain the stratigraphy of the Brushy Canyon Formation (Gardner et al., 2003, 2000). In stage 1 (*build*), there is deposition of unconfined flows bypassing the high gradient profile positions. This is followed by an erosive phase (*cut*) where sediment bypasses to the low-gradient profile positions provoking the collapse of sand banks. During the *fill* stage, the main phase of channel deposition occurs, and materials could be siliciclastic, carbonates or a mixture of both. Finally, after the channels are filled, deposition continues and either the channel is abandoned or re-initiated as multiple cut-fill-spill deposits.

Although conventional 3D seismic interpretation can provide an overview of the geomorphological elements of an area, amplitude-only analysis is cumbersome and not able to explain a depositional history in these complicated scenarios. The incorporation of seismic attributes enhances the reflection volume components that have an important correlation to the geological properties (Chopra & Marfurt, 2007; Zhao et al., 2016; La Marca-Molina et al., 2019). Modern software enables 3D manipulation of these attribute volumes to provide map and profile visualizations of the buried geological features, which then can be more easily interpreted as depositional environments. Previous studies of this area (Verma & Scipione, 2020; Bhatnagar et al., 2019; Yalcin et al., 2019) demonstrate how seismic multi-attribute analysis (geometric, instantaneous, and textural) highlights the depositional elements such as mass transport deposits and channelized features.

To complement the large-scale findings from the seismic interpretation, lithological analysis using well logs (sonic, photoelectric factor, neutron porosity, and bulk density) have been previously used with various semi-quantitative methods (e.g., ρmaa-Umaa) to determine the mineralogical composition of the rocks (Doveton,1994; Pranter et al., 2004; Dingmore, 2020). For the San Andres and Grayburg formations, the ρmaa-Umaa method has been previously used to determine the proportions of calcite, dolomite and quartz using as main input the bulk density, neutron porosity, and photoelectric factor logs (Pranter et al., 2004).

Although previous studies (He et al., 2019; Kvale et al., 2020) have integrated seismic geomorphology and lithology variation of hydrocarbon producing units of the Permian Basin, such as the Wolfcamp Formation, the San Andres and Grayburg formations in the Midland Basin remain overlooked, and a depositional model is required to improve the energy assessment of the area.

This research focuses on analyzing the lithological variations of the San Andres-Grayburg interval, its geomorphological evolution and how these two variables correlate in a depositional history. I build upon the work from Verma et al. (2023), Yalcin et al. (2019) and Yandell et al. (2019), who performed a multi-attribute analysis and lithological interpretation of the area of study and proposed the presence of siliciclastic channels in the Upper San Andres and Grayburg formations. However, studies integrating both components are absent due to data limitations (seismic resolution and lack of well data).This study employs a high-trace density (HTD) seismic survey with high resolution (90 ft; 27 m) that allows the creation of a 3D lithology model using as input results from two major stages: 1) lithological determination using the semiquantitative ρmaa-Umaa method with well-log data and calibrated with core, 2) geomorphological analysis based on seismic attributes (i.e., frequency, amplitude and geometric) for identification of the major architectural elements in the San Andres-Grayburg interval. Both results are integrated into a 3D lithology model using lithology logs (from stage 1) and spatial constraints (from stage 2). This integrated workflow is unique for the study area in terms of characterizing channelized features through the use of a high-trace density dataset enhanced with lithology from wells/core for stratigraphic interpretation.

Geological Setting

Basin history

The Permian Basin is in west Texas and southeast New Mexico covering an area of 115,000 mi^2 (~300000 km^2) extending over 52 counties (Fig. 1a). This basin is an asymmetrical, complex sedimentary system located in the foreland of the Marathon-Ouachita orogenic belt. It is bounded by the Marathon-Ouachita orogenic belt to the south, the Northwest shelf and Matador Arch to the north, the Diablo platform to the west, and the Eastern shelf to the east (Gardiner, 1990; Ewing, 1991; Hills, 1985). As observed, on Fig 1b, the seismic survey extends over the Central Basin Platform and the Midland Basin, which are two major tectonic features in this region, along with the Delaware Basin (Fig 1c).

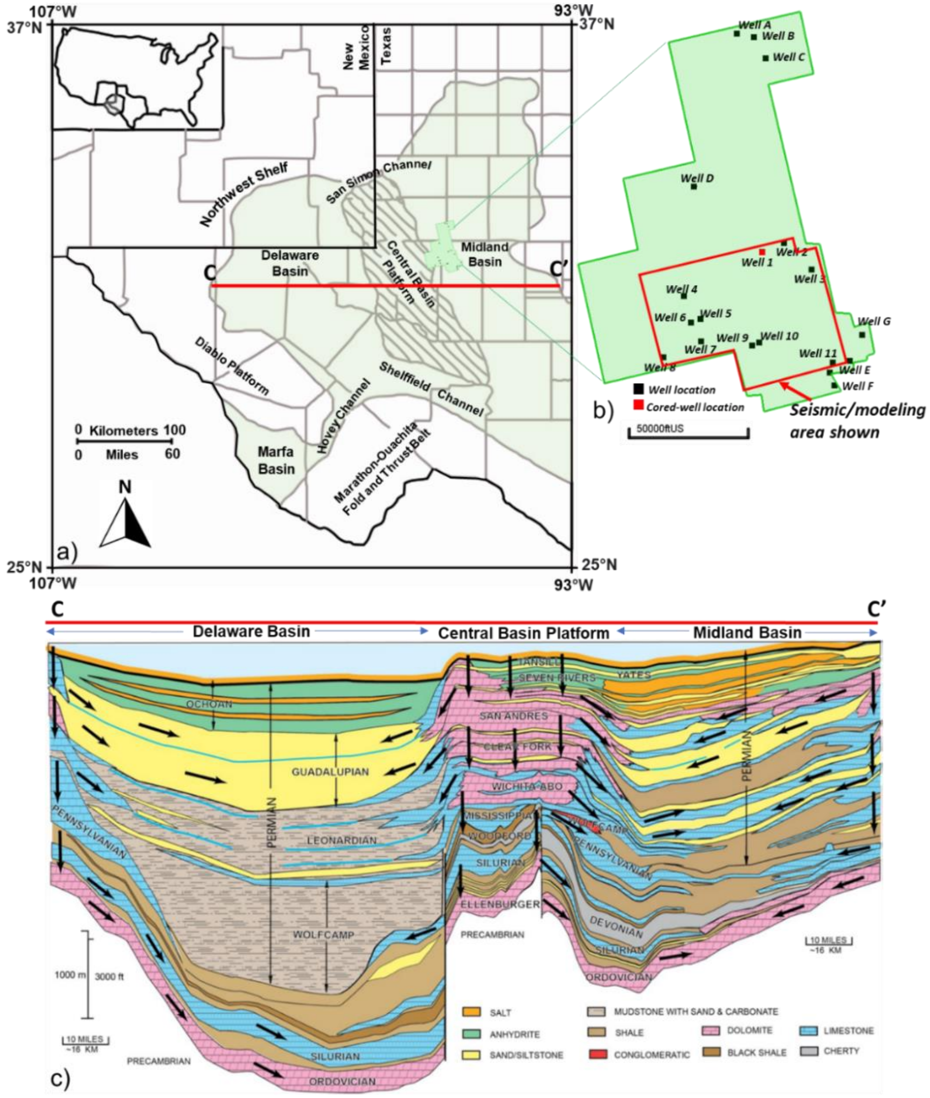

Figure 1. a) Location map of the area of study (seismic survey boundary) and structural components of the Permian Basin. Modified from Asmus and Grammer (2013). b) Seismic survey boundary with well location. Black dots denotate the location of the wells used in this paper, while the red dot represents the cored well location. c) Generalized cross-section of the Permian Basin. 2D view is exemplified on Fig 1a. From Saller & Stueber (2018), Matchus & Jones (1984).

Its depositional history can be divided into three major stages: 1) Cambrian to Mississippian, 2) Mississippian to Lower Permian and 3) Permian. Stage 1 (Cambrian to Mississippian) was characterized by passive margin tectonics with significant shallow marine deposition into the ancestral Tobosa Basin resulting in thick shelf carbonate and shale accumulations (e.g., Woodford and Barnett Shale). During the second phase, the collision of Laurentia with Gondwana resulted in the Ouachita-Marathon orogeny. This caused a relatively low-relief feature to be structurally uplifted during the middle to late Pennsylvanian which formed the present-day Central Basin Platform (CBP), separating the Delaware Basin from the Midland Basin. Significant siliciclastic deposition occurred as a consequence in these two basins, particularly during the Pennsylvanian (Atoka, Strawn, and Cisco formations). Simultaneously, an extensive development of reef facies accounts for a large percentage of the limestone deposits in shallow peripheral areas of the Delaware and Midland basins (Dolton et al., 1979; Hills, 1984). Lastly, the Permian stage accounts for several kilometers of sediment accumulated in the Delaware and Midland basins. Permian rocks are extremely heterogeneous, usually grading upward from a clastic-carbonate sequence into an evaporite sequence (Fig. 1c). Guadalupian, Leonardian, and Wolfcampian series consist of limestone interbedded with shale and minor sandstones (Oriel et al., 1967; Robinson, 1988). The cessation of tectonic activity and the transition to a stable marine basin fill-in stage influenced the depositional environment in Early Permian time. Clastic sediments were deposited in the Delaware and Midland basins, surrounded by peripheral reefs and carbonate shelves that graded shoreward into evaporitic lagoons. Target units of this article are the Guadalupian (Late Permian) San Andres and Grayburg formations.

Permian deposits (San Andres and Grayburg) are characterized by a period of transitional sea level cyclicity between high-amplitude (197 to 333 ft; 60 to 100 m) glacial-eustatic icehouse fluctuations of the Pennsylvanian and the low-amplitude (less than 32 ft; 10 m) eustatic greenhouse fluctuations of the Triassic (Barnaby & Ward, 2007). Paleogeographic maps support this characteristic showing an opening Tobosa basin, placed at 0˚ to 5˚ N latitude, as a consequence of the collision of Gondwana and Laurentia during the Middle Pennsylvanian, that is later filled with large accumulation of deltaic clastic sediments from the Ouachita orogenic belt. During the Permian period, the Midland Basin was covered with floodplains and nearly filled by the Middle Permian. The San Andres and Grayburg formations were deposited during a passive-margin phase of tectonic quiescence when arid conditions existed as indicated by dolomites, evaporites, eolianites, and terrigenous red beds (Meissner, 1972). The presence of shallow evaporites potentially affects the seismic quality of the interval of interest as waves propagate considerably faster over evaporites compared to siliciclastics. Additionally, salt has a larger reflection coefficient, reducing the energy that reaches the target zone, resulting in lower resolution.

Local stratigraphy

The Guadalupian San Andres and Grayburg formations consist of mixed carbonate-siliciclastic lithologies in the western Midland basin and were deposited in a ramp setting (Wilson et al., 2019). The ramp is primarily flat and homoclinal in the up-dip position and distally steepened to approximately three degrees in the down-dip direction (Lindsay, 2016).

These two units are subdivided into hierarchic successions of composite sequences (CS) and Permian high-frequency sequences (HFS) (Fig. 2a). The San Andres Formation extends from the Leonardian (L7/L8 high-frequency sequences, cf. Kerans et al., 2013 and Kerans & Ruppel, 2020) to early Guadalupian (G4) Lower San Andres Formation and the early Guadalupian (G8 and G9) Upper San Andres, which is overlain by the Grayburg Formation (G10/12) (Fig. 2a). The Lower San Andres (L7-G4) is composed of intercalation of shales and sandstones. During the deposition of the Upper San Andres (G8-G9), sea level rise led to aggradational to progradational cycles of ramp margin carbonates and basinal slope siliciclastic sediments (Mitchum & Van Wagoner, 1991; Fitchen, 1992; Kerans et al., 2013). The G9 HFS is identified by a progradational sequence of shelf clinoforms containing as much as 90% siltstone (Kerans & Ruppel, 2020), this lithology serves as source material for the channel filling in the Upper San Andres-Grayburg system. Limited accommodation space during the G-9 HST allowed generation of only erosional turbidites that were deposited along lower slopes of the progradational clinoforms (Sonnenfeld & Cross, 1993). Typical lithologies of the Upper San Andres in the western Midland Basin include carbonate-cemented siltstones that shoal upward into a series of cyclical fusulinid and ooid-bearing limestones and dolomites and anhydrite-bearing dolomites (Todd, 1976; Friedman et al., 1990). Finally, the Grayburg Formation (G10-G12), is characterized by dolomite and anhydrite deposits intercalated with some fine-grained sandstones and siltstones (He et al., 2019). The lack of clays in these basinal formations can be explained by detritus segregation in the eolian-marine model (Sarnthein & Diester-Haass, 1977; Sarnthein & Koopmann, 1980).

The cyclic deposition of carbonates and clastics in the Guadalupian-age units (Fig 2a) is explained by the reciprocal sedimentation model. In this model, there was rapid accumulation of a broad belt of carbonate and evaporites deposited on the ramp in playas, sabkhas and lagoons; coincident reef and or grainstone shoals deposited at the ramp margin; and thin and widespread carbonate turbidites collected in the basin during sea level highstand. Whereas in lowstands, fluvial and eolian terrigenous sands are deposited on the ramp and transported into the basin, probably down incised valleys and channels, to collect as very thick sandstone sequences (Van Siclen, 1958; Silver & Todd, 1969; Meissner, 1972) (Fig. 2b, c). My research focuses on understanding the dynamics of the channel incision during sea level changes that have been referred in literature as the *Midland Sands* (siliciclastics). As currently understood, these siliciclastic deposits originated in highlands located to the east, but the Central Basin Platform, Northern Shelf, and Eastern Shelf also supplied sediments to the basin during sea-level lowstands (Ward & Trentham, 2020).

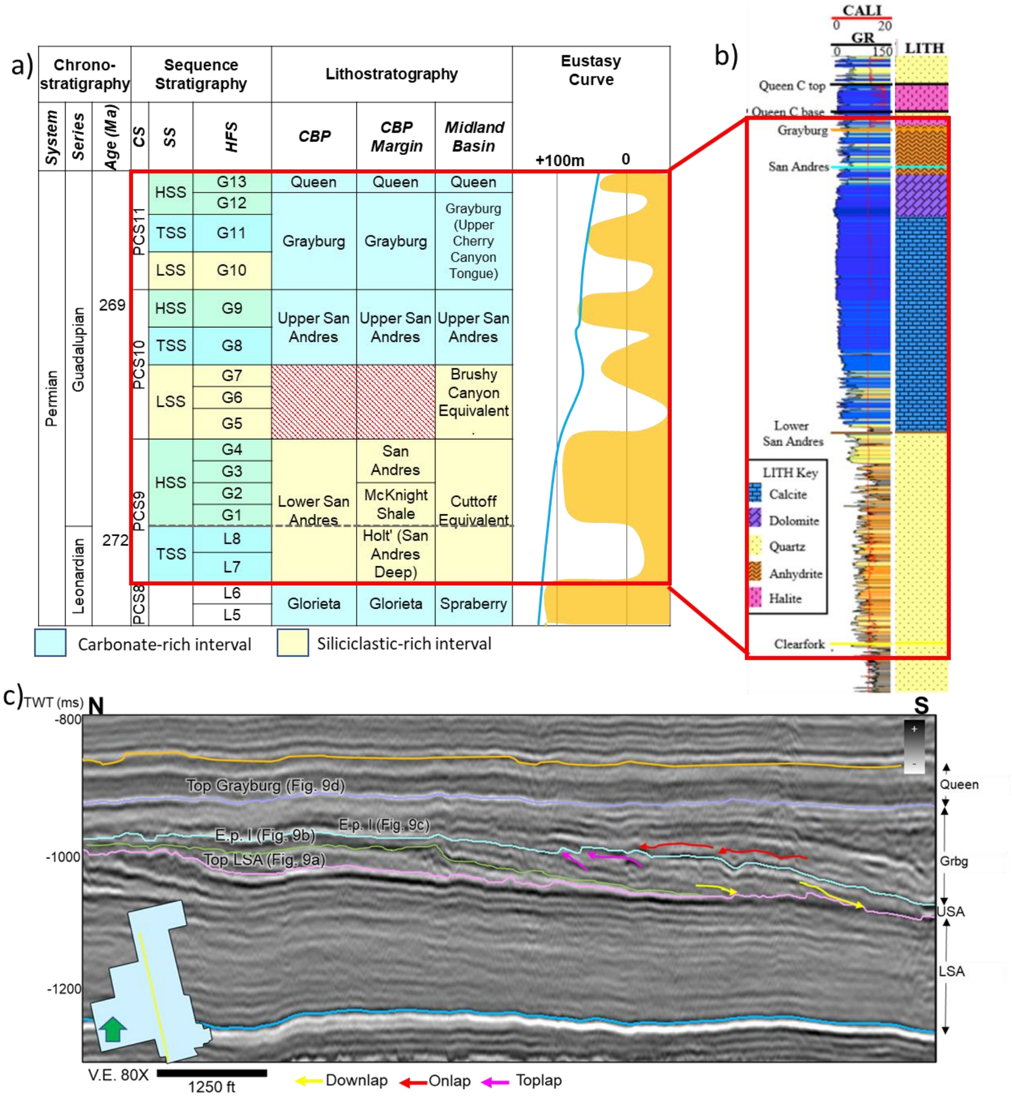

Figure 2. a) Stratigraphic chart of the Pennsylvanian and Permian units. Modified from He et al., 2019. CS: Composite sequence PCS: Permian Composite Sequence; SS: Sequence set,

HSS: Highstand SS, TSS: Transgressive SS, LSS: Lowstand SS; HFS: High-frequency sequence, G1–G13: Guadalupian 1–13 HFS ,L5–L8: Leonardian 5–8 HFS; HFC: High-frequency cycle Formation names. Dash-filled box represents an unconformity. b) type well log response of the interval of study (Wilson, 2019). GR = gamma ray log; CALI=Caliper log. The Lower San Andres is typically composed of siliciclastics (sandstones and shales), while in the Upper San Andres limestone and dolomite are dominant and the Grayburg is rich in evaporites like anhydrite. c) Local dip-oriented seismic section showing interpreted key surfaces and terminations. Location map on the left shows the top view of the section. Fig. 9. displays the map view of the surfaces pointed here.

Data

This study utilizes data from core, core descriptions, well logs, and high-resolution 3D seismic data.

Core

I evaluated 261 ft (79 m) of core from one well located approximately in the center of the study area (seismic survey outline) in the Midland Basin (Fig. 1b). The cored interval includes the Grayburg and Queen (overlies the interval of interest) formations.

Well logs

Logs from nineteen wells (Fig. 1b) are employed that included: caliper (CALI), gamma ray (GR), Spontaneous potential (SP), neutron porosity (NPHI), density porosity (DPHI), bulk density (RHOB), photoelectric factor (PEF), sonic (DT), and resistivity (RES). However, not all the wells contained all the previously mentioned logs for the section of interest and data increase was required to perform the further assessment of facies (see *methods and data conditioning section*). For the 3D lithology model, eleven wells were used (Fig. 1b). Some formation tops are also available for the units of interest (Grayburg and San Andres), which were used as guide for extending the interpretation.

Seismic

The CRanch 3D seismic survey is a post-stack time migrated volume that covers an area of approximately 280 mi^2 (725 km^2). It was acquired at the transition between the Midland Basin and the Central Basin Platform (Fig. 1a). It consists of 3242 inlines and 2333 crosslines with a stacking bin size of 41.25 x 41.25 ft (12.5 x 12.5 m) and a 2-ms sampling. Dominant frequency of the data ranges from 20-80 Hz and calculated vertical resolution at the depth of interest is approximately 90 ft (27 m). Therefore, shallow intervals will depict better small-scale geological features compared to greater depths. Nominal fold is 1024 within each 41.25 ft (12.5 m) bin, meaning there is a good distribution from near to far offsets reflected on the great resolution of the survey (Lewis et al., 2021). Appendix A compiles the acquisition information. Further details on the seismic acquisition can be found on Bhatnagar et al. (2019) and Lewis et al. (2021).

Seismic-stratigraphic framework of interval of study

The dip-oriented seismic section Fig 2c. shows the typical expression of the interpretation challenges of the interval of study as the variable clinoforms hamper the horizon picking. Applying reflection-geometry–based seismic-stratigraphic interpretation approaches (Mitchum et al., 1977), I first identified the shingled to sigmoidal reflections as clinoforms prograding toward the basin (north to south). These clinoforms terminate downdip (downlap) against a continuous and gently inclined seismic through at the toe of the slope; thus, I interpreted this reflector as the G9 base (Figure 2c). Meanwhile, these clinoforms seem to be terminated updip (toplap) against a relatively flat-lying seismic trough; thus, I interpreted this seismic trough as the G9 top (Figure 2C). G9 corresponds to the Upper San Andres

Formation. The upper-lying Grayburg Formation (G10-G12) is characterized by onlapping reflectors that terminate over the G9 top (red arrow, Fig. 2c). Reflector between the two formations marks a sequence boundary between PCS10-PCS11(He et al., 2019).

Methods and data conditioning

To better understand the data integration and multiple methods, Figure 3 summarizes the main workflow in detail as follows:

Core: lithology definition

No gamma ray measurements were run on the core to allow the correction for a depth shift (well to core tie). However, core descriptions (gross lithology) roughly match the well log interpretations, and therefore correlations between the two of these can be made qualitatively.

Well logs: rock type identification

Prior to the mineralogical calculations, a quality check workflow was performed to avoid miscalculations. Initially, the caliper log was inspected and in the interval of study, it was not above 13 inches (Dingmore, 2020). Samples taken in intervals at poor borehole conditions were not considered for the rock type identifications. Normally, these measurements tend to show outlier values in the well suite. Additionally, the sonic logs are de-spiked using a length of 15 and 2 standard deviations.

ρmaa-Umaa is a well-log based, multimineral, litho-density technique used to calculate the percentages of the main minerals. To perform this classification, a suite of logs that include DPHI, NPHI, PEF and RHOB is required. This multi-mineral technique calculates two parameters: ρmaa and Umaa from the bulk density, porosity logs and the photoelectric factor logs (Doveton,1994; Cluff et al., 2015). The ρmaa parameter is the apparent matrix grain density, calculated from the RHOB and porosity logs (Equation 1) and Umaa is the apparent matrix volumetric cross section (Equation 3), computed from the PEF log and the calculated photo-electron density constant (Equation 2). The two parameters are cross plotted on an imposed ternary diagram with trend lines for quartz, calcite, dolomite (QCD) and regions for clays and anhydrites. However, because these samples (every 0.5 feet) are mostly carbonates, the cross plot provides mineralogical estimates for quartz, calcite, and dolomite in volumetric proportion (%). Mud filtrate was assumed to be fresh water based therefore flush zone pore fluid density (ρf) and photoelectric absorption of the fluid (*Ufl*) are set to 1 g/cm3 and 0.5 barns/cm3, respectively.

$$\rho\text{maa} = \frac{\rho\text{b} - \phi\text{ta} * \rho\text{f}}{1 - \phi\text{ta}} \qquad (1)$$

$$\rho e = \frac{\rho_{b+0.1883}}{1.0704} \qquad (2)$$

$$Umaa = \frac{((PEF * \rho b) - (\rho e * \rho b)) - (\phi_{ta} * U_{fl})}{1 - \phi_{ta}} \; (3)$$

Where,

ρmaa = apparent matrix grain density (g/cm3)

ρb = bulk density (RHOB) (g/cm3)

ϕta= apparent porosity (v/v); this porosity is an average of the NPHI and DPHI.

ρf= flush zone pore fluid density (~1.0 g/cm3 for fresh-water mud filtrate)

Ufl=photoelectric absorption of the fluid

ρe = Electron density(g/cm3)

Umaa = apparent matrix volumetric

The samples were classified as so that if their mineral percentage was the highest (e.g., a sample with 60% quartz, 30% calcite and 10% dolomite is classified as sandstone). Shales were identified using a GR cutoff of 65 API (higher than).

Out of the nineteen wells, nine had this well log combination for the interval of interest, the rest did not include photoelectric factor logs (PEF). However, because the purpose of this project is to obtain a regional view of the area, I used the existing logs to train an artificial neural network (ANN). The best model results were obtained from inputting a well log suite composed of sonic (DT), Gamma-Ray (GR), Neutron Porosity (NPHI) and Bulk Density (RHOB). The model was trained using six of the nine wells and validated on two of the other wells with PEF to check its accuracy. Validation was only performed qualitatively, and it proved to be successful at representing the general trends.

Seismic

The original seismic was preconditioned to reduce noise by applying structural-oriented filtering (Zhang et al., 2016; Guo et al., 2018; Ray et al., 2022). The filtered dataset was used as input for multiple seismic attributes: geometric, instantaneous, and frequency based. Additionally, the pre-conditioned data were utilized for horizon interpretation. Three key surfaces were picked manually: 1) Top of the Glorieta/Base of the Lower San Andres (peak), 2) Top of the Lower San Andres (trough) and 3) Top of the Grayburg (trough). Additional horizon interpretation, such as the Top of the Upper San Andres or the base of certain key internal events were obtained from automatic stratal slicing (Fig. 2c).

Initially, conventional amplitude-seismic interpretation was used to have an overall idea of the lithological changes based on impedance contrast. Cross-sections and horizon slices indicate that the interior of the channelized features exhibit continuous low amplitudes along strike. This is a consequence of an acoustic impedance contrast between the infill material and the surrounding lithology. As a general assumption, sandstone has lower acoustic impedance relative to carbonates as it is a lower density material. However, to enhance the interpretation, multi-attribute analysis was implemented, and three different types of attributes (geometric, amplitude-accentuating and frequency) were used to better understand the deposits. Selected attributes were chosen due to their proven usefulness in other seismic studies in similar settings.

Morphological characteristics are effectively imaged by geometric attributes such as dip magnitude and azimuth, apparent dip, coherence, structural curvature and coherent energy. These are excellent edge-detection tools and are especially helpful in defining geobodies with sharp margins such as channel margins, reef belts and carbonate mounts (Posamentier *et al.*, 2007). Dip magnitude, θ, is identical to that used in the above geologic definition (measured from the flat surface at the maximum inclination point of a plane). Complementary, dip azimuth, is measured either from the north, or for convenience, from the inline seismic survey axis. Dip azimuth is perpendicular to the geologic strike and is measured in the direction of maximum downward dip (Chopra & Marfurt, 2007). Apparent dip, similar to the concept of dip magnitude, measures inclination of the reflectors relative to an orientation from the north/inline direction (e.g., 30, 60…) instead of the maximum inclination. This is applied in settings where the interpreter aims to highlight structural or stratigraphic features perpendicular to that direction (e.g., channels as in this case) (AASPI documentation, 2022). I used a sobel filter as the coherence algorithm because, unlike most of the coherence algorithms (e.g., eigenstructure coherence), sobel filter detects the changes in amplitude and waveform, instead of only changes in the waveform shape. Therefore, a subtle channel (like in this case < 150 ft [~46 m] deep) would not show any eigenstructure coherence anomaly but may have a strong sobel filter response (Verma et al., 2022). Curvature measures how bent a curve is at a particular point on a two-dimensional or three-dimensional surface, highlighting paleo-lows or highs (Chopra & Marfurt, 2007). The coherent energy attribute measures the coherent part of energy in the seismic that exhibits the same waveform along the structural dip in a chosen computation window and it was applied to enhance the visualization of channel in fills (Verma et al., 2022).

Frequency attributes, such as peak magnitude or peak frequency, are generally associated to amplitude accentuating ones as bed thickness (i.e., reflector frequency) is related to the dominant lithology (e.g., thick sandstone intervals exhibit low frequencies and high amplitudes) (Koson et al., 2014). Peak magnitude is defined as the maximum value of absolute values of amplitudes in a specific window while peak frequency is the dominant frequency in during 1-second sampling (La Marca et al., 2019). Some of the common uses of peak spectral frequency and magnitude are the differentiation of thick from thin channels, and over bank deposits (Zhao et al., 2016). Spectral components co-rendering (spectral decomposition) is also helpful on channel morphology studies. This technique aids in representing changes in thicknesses (high frequencies represent thin bedded deposits while low frequencies do the opposite) as it separates the full bandwidth seismic into the desired frequency components. Generally, results are displayed in a RGB (red-green-blue) blending that co-renders a low, middle, and high frequency. Applications of this technique include improving channel body continuity, fill variability, and possible reservoir quality (Peyton et al., 1998, Chopra & Marfurt, 2016; Zhai & Pigott, 2021). The spectral decomposition method chosen was continuous wavelet transform (CWT) after comparison with the Short Time Fourier Transform (STFT).

Amplitude-accentuating attributes (e.g., sweetness, relative acoustic impedance, amplitude curvature) are primarily implemented as lithology indicators that are useful in detection of potential conventional reservoirs as boosts sand-rich deposits (Sacrey & Roden, 2014; Zhao et al., 2016). One of the most successful amplitude-derived attributes is amplitude curvature. It is defined as the second-order derivative of time or depth structure or a 2D first-order derivative of inline and crossline dip components. The most popular application of this attribute is channel imaging where reflector bending is not significant to be depicted by the structural curvature (Chopra & Marfurt, 2013; Verma et al., 2022). Sweetness, an indicator of the infill variability, is calculated by dividing the instantaneous amplitude (amplitude envelope) by the square root of the instantaneous frequency. Areas containing higher amplitudes and lower frequencies (sandy intervals) will display the highest values for sweetness, while lower amplitude and higher frequency sediments (thinly bedded shales) will show lower values for sweetness (Hart, 2008).

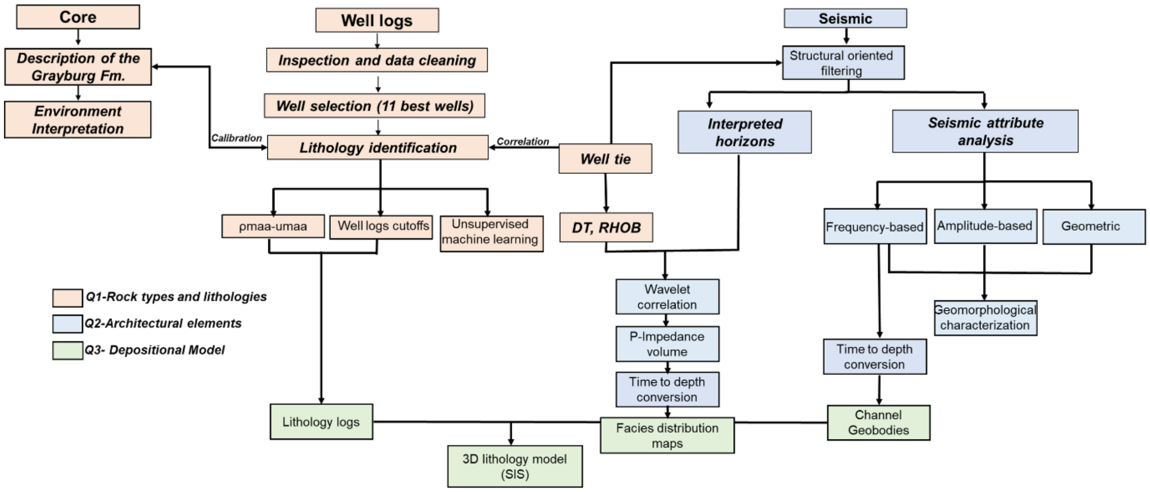

Figure 3. Workflow of the study. The processes are color coded according to their contribution to answering the research questions.

Channel geobody extraction and time to depth conversion

In order to integrate the seismic as an aerial constraint for the 3D modeling, I used the methodology recommended by (Sanchez et al., 2018) and (Santana & Elizondo, 2019) which uses the spectral components co-rendering (RGB) as input for identification, interpretation and extraction of geobodies (e.g., channels). This workflow is divided in three steps: 1) selection of the best spectral components by inspection of the frequency spectrum, 2) interpretation of geobodies by polygon drawing and 3) geobody extraction. These geobodies represent the channel fills where according to initial observations are the most likely to be sandstone filled.

To tie the geobody work to the petrophysics in the 3D lithology model, I built a velocity model using time-depth relationships (TDR) established from the seismic-to-well ties of ten wells. Four horizons (top of the Glorieta, top of Lower San Andres, top of Grayburg and top of Queen Formation) in time were used along with the 40 well tops in 10 well locations to perform the conversion following this model (equation 4):

$$z = Z_r + v_0(t - t_r) \text{ (4)}$$

Where z is the calculated depth of the point, zr, the depth at the well location, v0 the calculated velocity and (t-tr) the difference in time.

As a result, depth structure maps of the time surfaces were obtained, some of which were employed as zone limits. Other seven-time surfaces were converted into depth using the model. This time to depth model, was also utilized to convert seismic attribute volumes when required.

Post-stack inversion and rock type probability map generation

In other to constrain the lateral facies distribution during the 3D modeling process, I explored the relationship between acoustic impedance and lithology. A general relationship was observed between various ranges of well-log-based p-impedance values and rock types (Appendix Ba). Unlike in other areas (Dingmore, 2020; Turnini, 2015), where each of the rock types has a discrete range of the acoustic impedance, my interval of study shows considerable overlap in between facies; especially in between the limestone and dolostones. However, each rock type exhibited a negative relationship between increasing p-impedance and decreasing porosity; this general relationship was used to generate facies distribution and probability maps (Appendix. Bb) which were used to constrain the spatial distribution of lithologies between wells during the modeling process. Figure 4 summarizes the workflow followed to employ the acoustic impedance for lithology prediction.

A model-based post-stack inversion was performed to derive a 3D p-impedance volume (Fig.4). Essentially, this process consists of integrating post-stack seismic with well log data to estimate acoustic impedance, which gives hints of lithology and porosity variations. I used model-based inversion to calculate the acoustic impedance volume, (P-impedance). This method states that the seismic trace can be generated from the convolution of wavelet with the Earth reflectivity. Assuming the seismic ray of incidence is at a normal angle to the rock interface, the reflection coefficient (Ri) is equal to the p-impedance. The post-stack inversion reverses the forward modeling procedure by deriving an impedance volume from the reflectivity (Maurya & Sarkar, 2016). To perform a model-based inversion, an initial geologic model (also known as low frequency model) is built from the interpreted horizons and low frequency filtered impedance logs by extrapolating the impedance values throughout the volume using the horizons as spatial constraint (Fig 4). The extrapolation is done by weighting the log values inversely proportional to the square of the distance from wells. Next, a synthetic trace is generated by convolving the model values with a wavelet and it is then compared with the equivalent seismic trace (Caf, 2022). This process is altered iteratively until the difference between the inverted trace and the seismic trace is reduced to a threshold value. A model with a very small difference is accepted as a solution (Veeken & Da Silva, 2004).

Three wells strategically distributed were used: Well 9 (penetrates channel), well 1(cored well) and the Well 5 (Fig. 1). These wells were selected based on their quality of density and sonic logs (no outlier, linear trend, etc.). Some of the different settings explored were:

Types of wavelets:

- extracted along the well path, phase rotation average of 100°

- Statistical complete volume
- Statistical Queen to Marker

Windows of inversion:

- Complete volume: top of the Glorieta to top Queen
- Top of LSA to top of the Queen
- Marker (reflector between Upper San Andres and Grayburg) to top of the Queen

Iterations: 5 or 50. Plot shows that P-impedance error increases after 5 iterations (Appendix C).

The best P-impedance volume is then converted to depth and upscaled to the model grid to observe the distribution per zones. As previously mentioned, the rock types in the area of study had no discrete acoustic impedance ranges, and the correlation between P-impedance vs porosity (Appendix Bb) was used discriminate rock types. Therefore, a total porosity model was built from the available wells using a cloud transform. To accomplish this, I used the p-impedance vs porosity cross plot at the well scale correlation as a cloud transform with ten equally spaced bins. Using sequential Gaussian simulation (SGS) the porosity modeling is performed using a bivariate distribution method being the secondary property the upscaled p-impedance volume and guided by the p-impedance vs porosity cloud transform. Variograms were set to isotropic (20000 ft; 6000 m) for all the zones. The porosity and p-impedance volumes are then cross plotted and using the rock type trends observed I manually selected 3 polygons that represent each of the facies (Fig. Cb). The polygons create a filter in the 3D model that was used to extract a volume of limestone, dolostone and sandstone for each zone. Then, proportion maps were calculated by dividing the facies thickness per zone by the total thickness of each zone. These proportion maps represent the probability of encountering each lithology and are used as an additional constraint for the facies modeling. This workflow involves a considerable uncertainty due to 1) quality of the inversion, proved to be inconsistent in the northeastern part of the survey (Wells 1, 2 and 3) and 2) manual selection of the facies polygons over the P-impedance vs porosity cross plot. Further adjustment in the post-stack inversion is suggested.

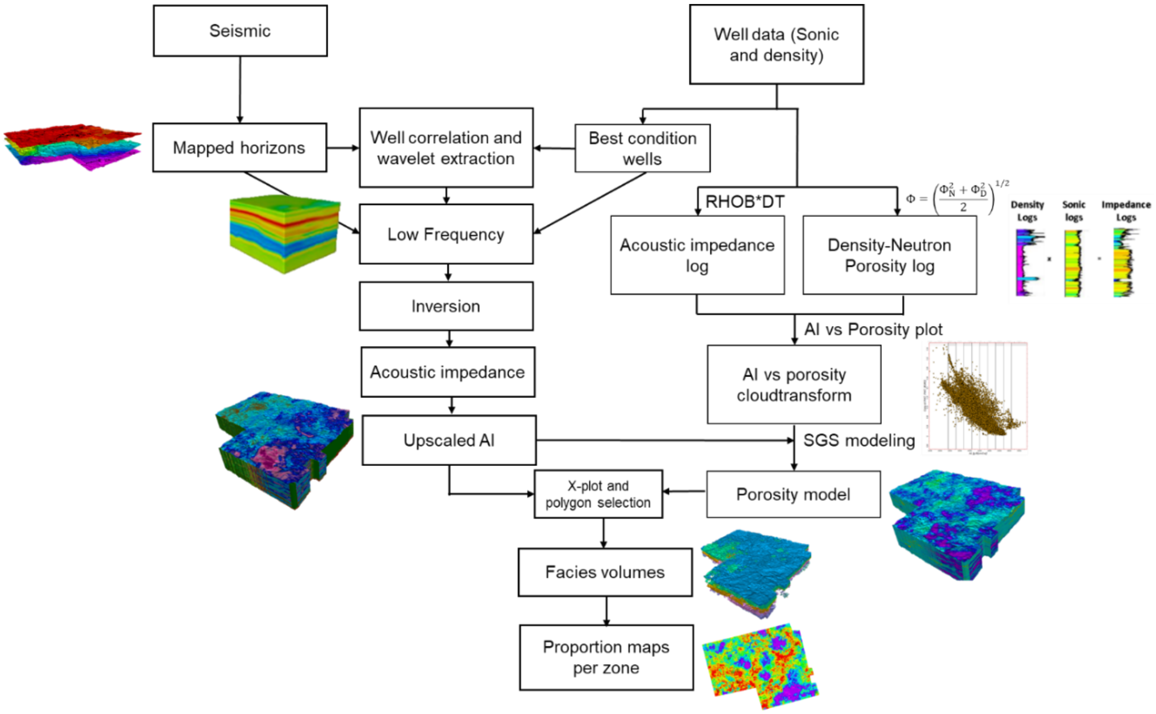

Figure 4. Generalized post-stack seismic inversion workflow and proportion maps generation (based on Farfour et al., 2015).

Facies modeling

A 3D lithology model was built using sequential indicator simulation (SIS) to understand the spatial distribution and geomorphological evolution of the lithologies and channels in the area. The grid dimensions were determined based on various factors like the average distance between wells and dimensions of the channels, and the vertical resolution was set to preserve the stratigraphic variability of rock types while maintaining an adequate number of cells of computational purposes (150i x 150j [ft]). Ten stratigraphic surfaces that were interpreted for the San Andres and Grayburg fomations were used to define nine zones (A-I, being A the youngest and I the oldest) that comprise the Upper San Andres and Grayburg formations to depict properly the clinoform geometries of the area of interest (Fig. 5a, b). Within each zone, proportional layering was used for the stratal geometry. The number of layers for each zone was chosen depending on the level of detail required. Zones E and F(Upper San Andres and Lower Grayburg), which include the channelized intervals, had additional detail (15 layers) while the rest were kept at 10 layers (Fig. 5c). Due to the clinoform structure, cell thickness varies along the direction of progradation (Fig. 2c). The grid was quality checked by comparing if the grid covers properly the channels observed in seismic in both vertical and horizontal directions.

As a first step, the lithology logs calculated from the ρmaa-Umaa analysis were upscaled to the model grid. The accuracy of the upscaling was validated by comparing the original and upscaled logs with frequency histograms (for rock-type proportions) and cross sections (for rock-type presence).The lithology model was modeled using sequential-indicator-simulation (SIS) constrained to the (1) stratigraphic framework (3D grid), (2) upscaled lithology logs (Appendix D), (3) vertical lithology proportion curves (Appendix E), (5) vertical and horizontal variogram parameters by lithology and zone (Appendix F), (6) geobodies for the channel fills (sandstones) and (7) probability maps for each zone for each lithology: limestone and dolomite. Because the probability maps are based on the seismic which provides guidance for the lateral lithology distribution, the range for major and minor directions of horizontal lithology variogram parameters was set to 20,000 ft (6000 m) for all the lithologies and all the zones. Vertical ranges for lithologies were set based on the data analysis of log data (Appendix F).

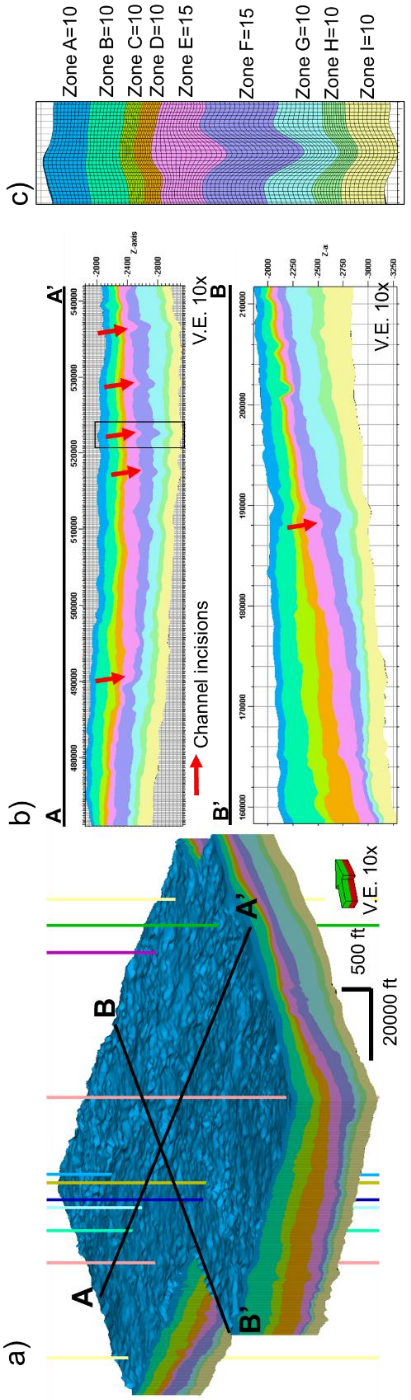

Figure 5. a) 3D reservoir model grid of the Grayburg and San Andres Formation. Automatic extracted horizons were used as boundaries of each zone (9) and proportional layering for the stratal geometry. B) Cross-sections parallel and perpendicular to the C) Cell dimensions purposely selected to capture geological variability. The 3D reservoir model grid contains cells with dimensions of 150 X 150 ft (I and J directions),100 layers of different thickness (K direction of 10 ft in the thickest portion), for a total of 32967000 cells. Number of layers per zone are specified as well.

Results and Interpretations

Core descriptions and depositional environment interpretations

As previously discussed, the available core covers the Queen and Grayburg formations. A detailed facies analysis was undertaken for the Grayburg Formation to identify the lithofacies and to interpret the environment of deposition (Fig. 6). Table 1 summarizes the characteristics of each lithofacies. The petrophysical results section expands upon the application of the core descriptions.

Calcareous Siltstones (SLca, Sca)

These facies are typical of the Upper Grayburg and varies from massive calcareous argillaceous siltstones into laminated (Fig. 6a). The massive facies contain chert nodules and rip-up clasts, while laminated are a fine intercalation of argillaceous (dark) to calcareous silt (light). Exposure surfaces are common on this interval. Both facies are presumably dolomite-cemented based on its weak reaction to HCL. Other characteristic features of the calcareous siltstones, especially at the very top of the Grayburg, are the algae laminations and evaporite layer intercalation. Based on these facies' association, I interpreted this interval (4850-4920 ft) to have been deposited in tidal flats and continental sabkha (4800-4850 ft).

Dolostone (Dk, Dpf)

Dolomitic facies are common in the middle Grayburg and are characterized for different types of porosity and are impregnated with hydrocarbons (residual oil zone-ROZ). The upper part of the middle Grayburg tends to have karstic porosity and fractures filled with hydrocarbons (Fig 6b). Some areas have a breccia-like appearance with different crystal shapes (elongated, tabular). Sulfur crystals of up to 8 centimeters are scattered throughout the karstic interval as a result of the karst overprint within the residual oil zone-ROZ. The base of the middle Grayburg instead is porous but not karstic (Fig. 6c) and unlike in the karstic dolostone bio-clasts are frequently found, especially crinoids. Crinoids are bathymetry indicators and related to a sea level drop as crinoid mud mounds are developed at 40-80 ft (12-24 m) of water.Therefore, environment interpretation suggests a shallow marine with episodic aerial exposure.

Packstone (Pff)

Packstone facies are restricted to the lower portion of the Grayburg Formation and characterized by its fusulinid content (Fig.6d). Unlike the crinoids, fusulinids are bathymetry proxies of sea level rise and related to transgressive cycles.

Crinoid-supported packstones are stratigraphically above the packstone facies suggesting sea level fall episodes.

Wackestone (Wsf)

Wackestone (Fig. 6c, e) are similar in composition to the packstone, but fossil content is considerably less (<10%). Grains are a mixture of crinoids, fusulinids and shells. Some carbonate mud laminations are observed in the middle Grayburg, although the wackestones are generally intercalated with packstones and formed as result of changes in the water conditions (oxygen level, depth, etc.) that indicate not appropriate settings for the organisms. This lithology relates to relative sea level rise.

Fine-grained sandstones (FSm)

These facies are constrained to the base of the Grayburg Formation. Massive with some bioclasts embedded (shell fragments, crinoids). Fine grained sandstones (that occasionally transition into siltstone) are often described intercalated with evaporites as a result of regression.

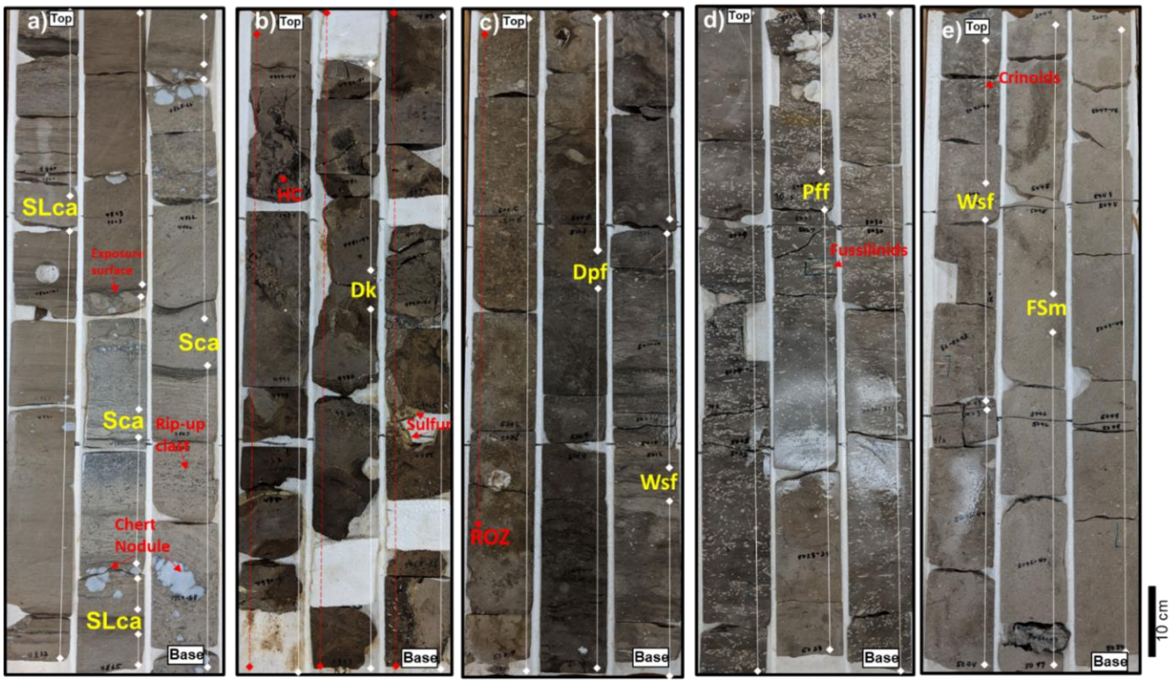

Figure 6. Core photographs of the different facies in the Grayburg Formation. Cored well location is depicted on Fig 1. Interpretations and further descriptions are shown on Table 1 and Figure 8. (a) 4860-4869 ft Calcareous argillaceous siltstone alternating from massive to laminated. Sedimentological features such as rip-up clasts and chert nodules are common. (b) 4977-4985 ft. Dolomite with karstic porosity (Dk). Hydrocarbon-filled fractures and sulfur crystals of approximately 5 centimeters are typical in this section. This interval is part of the residual oil zone (ROZ). (C) 5004-5013. Porous dolomite with fragments (Dpf) and the wackestone with shell fragments (Wsf). (d)5022-5032 ft Packstone with fusulinids fragments (Pff) (e) 5041-5049 ft. Wackestone (Wsf) and fine-grained sandstones (FSm). Bioclasts of crinoids and shells are commonly found in both lithologies.

Table 1. Petrographic compilation of most common facies found in the Grayburg Formation.

Facies	**Sedimentological features**	**Interpretation**	**Rock type**
Massive fine sandstone (FSm)	Massive, a few scattered fragments.	Sea Level Fall	Sandstone

Wackestone with shell fragments (Wsf)	Massive to laminated, with some crinoids and shell fragments.	Sea Level Rise	Limestone
Packstone with shell fragments and crinoids (Psf)	Dark gray and massive with abundant shell fragments and crinoids.	Sea Level Fall	Limestone
Packstone with fusulinids fragments (Pff)	Dark gray and massive with abundant fusulinids.	Open Marine, Sea Level Rise	Limestone
Porous dolomite with fragments (Dpf)	bio-clasts are frequently found, especially crinoids.	Sea Level Fall	Dolostone
Dolomite with karstic porosity (Dk)	Highly fractured rock and hydrocarbon filled. Sulfur crystals are common as well as dissolution.	Karstification, Sea Level Fall (Exposure)	Dolostone
Calcareous argillaceous siltstone (Sca)	Rip-up clasts and chert nodules are common,	Sea Level Fall, Tidal flats	Dolostone/Sandstone
Laminated calcareous argillaceous siltstone (SLca)	Areas of slightly enriched (darker) or depleted (lighter) clay content.	Sea Level Fall, Tidal flats	Dolostone/Sandstone

Petrophysical analysis

Figure 7a and 7b show the structure and dominant lithologies of the units of interest. The Lower San Andres tends to be siliciclastic dominated (shales and sandstones) with considerable dolomite and calcite detrital fragments that grade upward into limestones and dolostones in the Upper San Andres. The Grayburg Formation is generally composed of sandstones at the base that grade upwards into the limestones and anhydrite-bearing dolostones. For this study, I did not invert for anhydrite as it is a minor mineral. But generally, if non classified samples are present in the Upper Grayburg it is due to considerable anhydrite percentage. This interpretation agrees with generalized descriptions of the San Andres-Grayburg interval in the Midland Basin: lower, terrigenous clastic zone containing dolomite- and calcite-cemented siltstones that grade upward into a series of cyclical fusulinid and ooid-bearing limestones and dolomites and anhydrite-bearing dolomites (Todd, 1976; Friedman, et al., 1990; Wilson et al., 2019). Fig. 8 serves as a quality check of the correlation between the lithofacies and the lithologies obtained at the well-log scale.

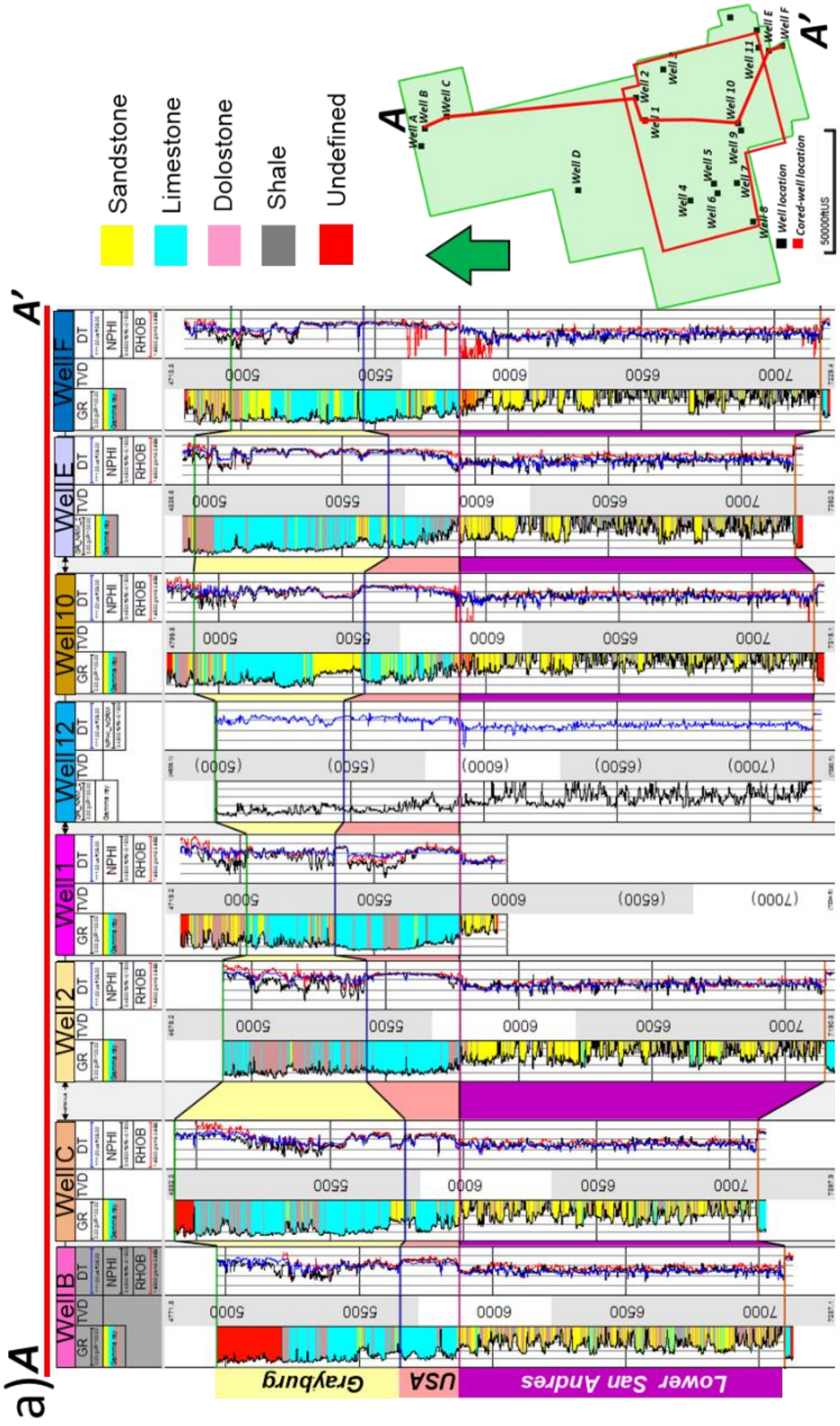
a)
A
A'
Well B
Well C
Well 2
Well 1
Well 12
Well 10
Well E
Well F
GR
TVD
DT
NPHI
RHOB
Grayburg
USA
Lower San Andres
5000
5500
6000
6500
7000
Sandstone
Limestone
Dolostone
Shale
Undefined
Well A
Well B
Well C
Well D
Well 1
Well 2
Well 3
Well 4
Well 5
Well 6
Well 7
Well 8
Well 9
Well 10
Well 11
Well E
Well F
Well location
Cored-well location
50000ftUS

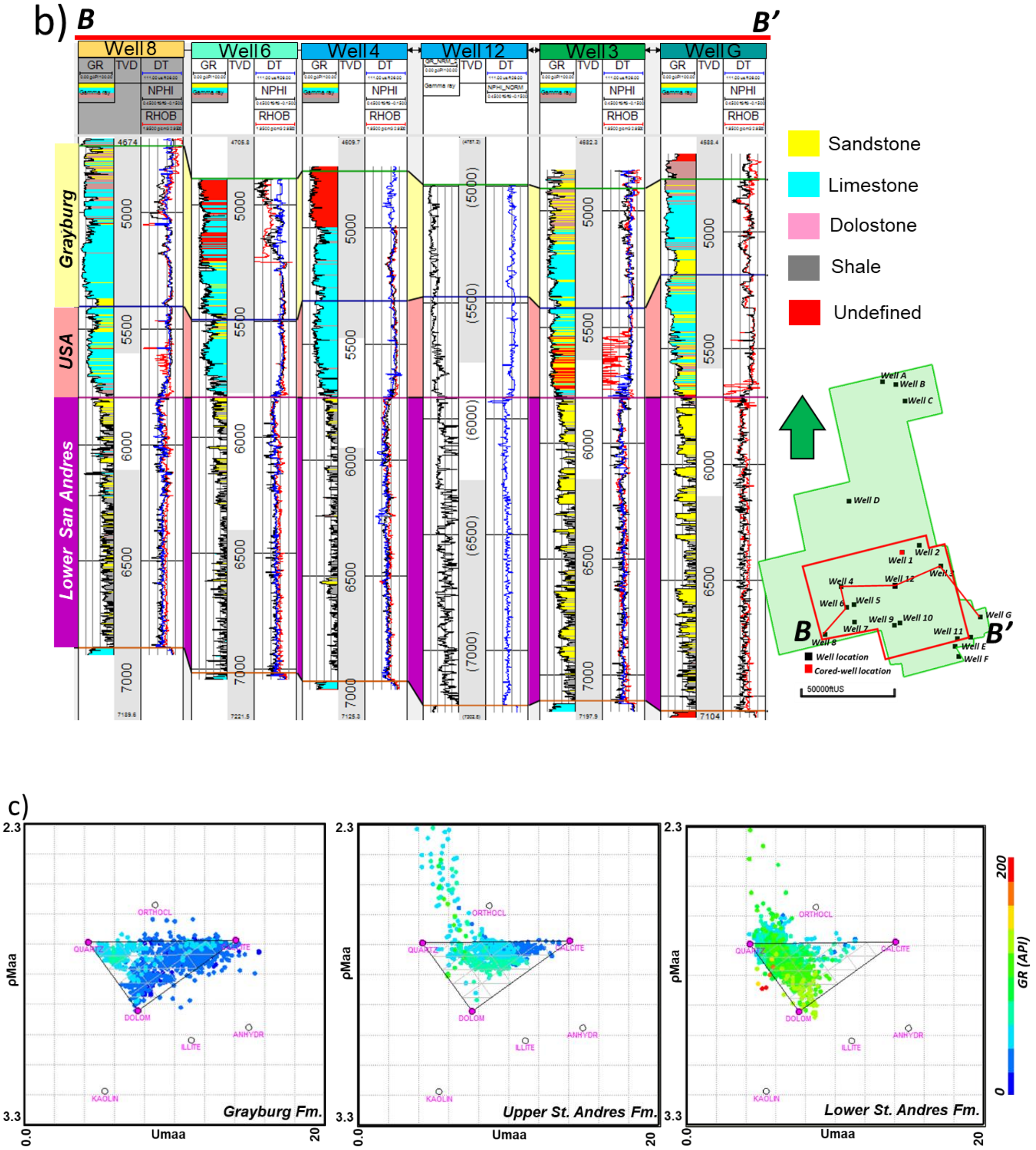

Figure 7. a) NS and b) WE well sections of the San Andres and Grayburg formations displaying some of the most relevant well logs (GR, DT, NPHI, and RHOB). The section was flattened over the Lower San Andres top. Location map of the wells is shown to the right as well as the 2D cross-section view. GR track has been color-coded accordingly to the interpreted facies from the ρmaa-Umaa method. Abbreviations,USA= Upper San Andres. Here the plotted tracks are, track 1 GR: 0 to100 API black curve, Pmaa-Umaa facies as color filled from the curve to left edge of the track; track 2 TVD in feet; track 3, DT:111 to 26ms/ft blue curve, NPHI:45 to -15% black curve, RHOB: 2 to 3 g/cm3 red curve. C) The ρmaa-Umaa cross-plots per unit illustrates the stratigraphic variability of mineral composition for the Grayburg, Upper San Andres and Lower San Andres Formation. Each unit exhibits a

distinct mineralogy (rock type) as interpreted from the proximity to the ternary plot vertexes, i.e., the Grayburg (dolomite; dolostones with some calcite, limestones), Upper San Andres (calcite; limestone) and the Lower San Andres (quartz; sandstones, and shales).

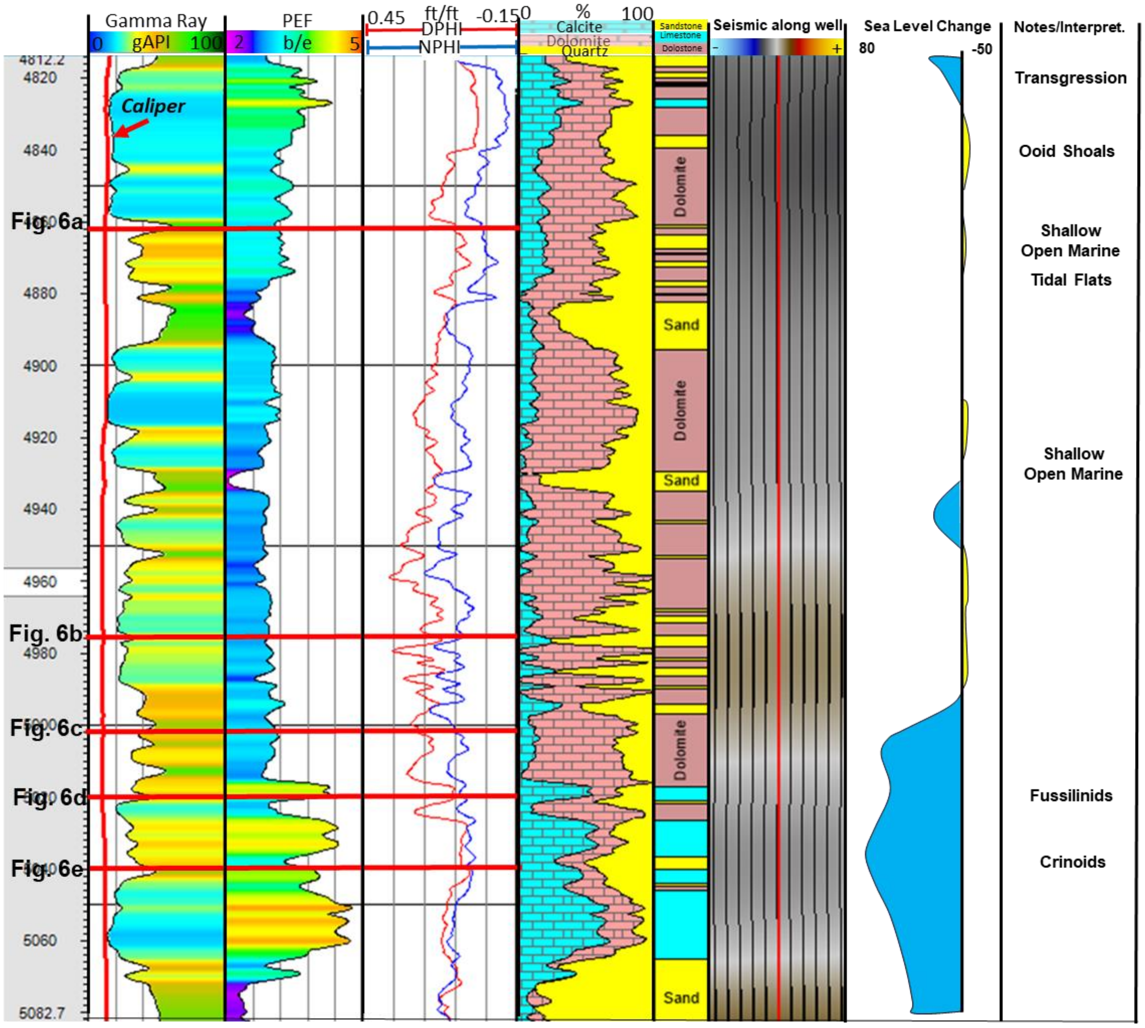

Figure 8. Cored well suite of logs (GR, PEF, DPHI, NPHI, DT) of the Grayburg Formation with ρmaa-Umaa mineral percentages and the correspondent rock type interpretation. The lithology log shows three rock types (sandstone in yellow, limestone in cyan and dolostone in pink). The seismic along the well path shows the reflective behavior, positive amplitudes are associated to increases in impedance (denser rock) while the troughs are indicators of opposite lithologies. In this figure it is difficult to find a correlation between the seismic and the lithologies as the resolution is of ~90 ft and changes in mineralogy/porosity are seen a smaller scale at the core. Additionally, I show the sea level interpretation by Lee et al. (2018) and important notes/environment interpretation. Location of core pictures (Fig. 6) are also shown to reference its stratigraphic position.

Seismic stratigraphy

Stratal slicing output was used to map intraformational reflectors (peak, through and zero-crossing) to understand the changes in the paleo-geography and its effects on the deposit's lithology (Fig. 9). The base of the lower San Andres shows a structural high to the west of the AOS related to the Central Basin Platform carbonate development in the underlying strata (Glorieta Formation) and deepens east-ward. Internally, the Lower San Andres has near-planar reflectors that only deepen to the west due to the CBP structure. The top of the Lower San Andres (Fig. 9a) shows that the depocenter has moved towards the south and linear features, presumably channel incisions, are seen proximal to the depocenter, suggesting that the shelf margin follows the perpendicular direction (west to east). The Upper San Andres top, and the internal reflectors, evidences the same trend of the Lower San Andres top, where the depocenter continues moving southward (Fig. 9b). Amplitude sections (Fig. 2c) support this observation, as the reflectors terminate downlapping over the lower San Andres top and top lapping against the Upper San Andres as shingled to sigmoidal reflections interpreted as clinoforms prograde towards the basin (yellow arrows). The maximum dip of the clinoforms is around 5°, measured in the depth-converted data. The Grayburg time structure indicates no such trend of change in elevation as the previously described surfaces (Fig. 9d). Onlapping was also observed in the Grayburg Formation over the Upper San Andres top as surface in between. Detailed mapping is crucial to understand where is most likely to find the channel incisions as the shelf position determinates their development.

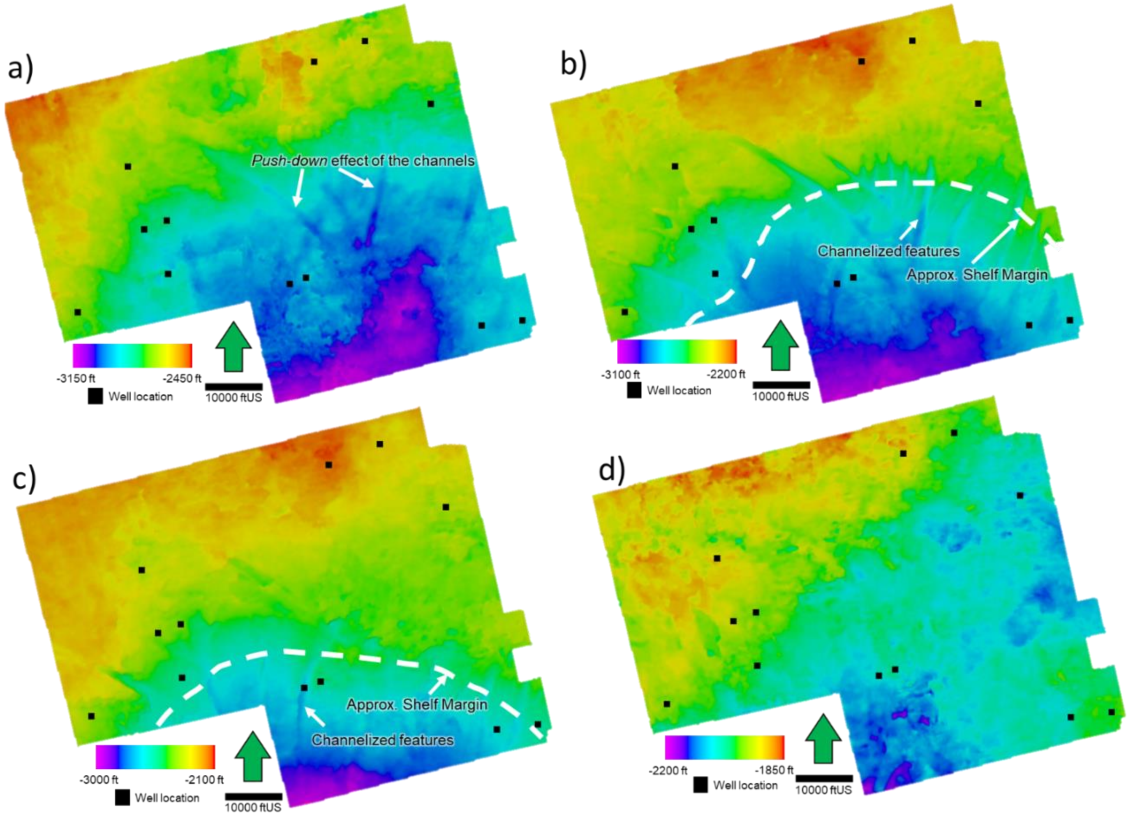

Figure 9. Depth converted time structure maps of the key horizons in the Upper San Andres and Grayburg. Surfaces are cropped to the model boundary (Fig. 1b). (a) LSA (Lower San Andres Formation top, (b) Channel episode I occurred during the Upper San Andres, (c) Channel episode II occurred during the Grayburg, (d) Grayburg Formation Top. Note that, the warmer colors (red-orange) correspond to the shallower depths while the colder colors (blue-purple) indicate the deeper depths. Seismic stratigraphic location of the surfaces is shown on Fig. 2c for reference. Some features such as the shelf edge interpretation and channels are pointed as well.

How do seismic attributes help characterize incised channels?

To investigate the geomorphological history of the submarine channels in the deeper unit, the attribute extractions were performed over two key surfaces (Upper San Andres Top-intraformational top X1 (Fig. 9b) and Grayburg Intraformational top X2 (Fig. 9 c)) that correspond to channel episode I and II, respectively. In the area, at least five major channel erosion events occurred during deposition of the San Andres and Grayburg formations.

Dip azimuth (Fig. 10a, b) displays the direction of dip relative to the north and evidence that channelized features located over the shelf break are prominently dipping back and forth in an east then west alternating pattern (Fig. 10a), this intrinsically suggest a V-shaped type of channel versus a U-shaped where the center of the channel has low angle (N-S) orientation (Fig. 10b). The dip gradient attribute shows the changes in dip (structure) along an assigned direction relative to the north (30°, 60°, etc.). This attribute provides a *paleo-topography* view, exposing two main trends of channel strikes: NW-SE and NE-SW (Fig. 10c, d). Similarly, the structural curvature attribute supports the structure observations on the dip gradient attribute as channel fills are represented by the negative anomalies while the channel edges have an opposite response (Fig. 10e, f). Co-rendering of coherent energy and coherence unlike the other geometric attributes indicates variations within the channel features. It shows medium to high values inside the channels that contrast with the low values of the shelf. This is particularly observed in channel episode I (Fig. 10g), where high values over the basin floor (south) potentially correspond to splays or laterally continuous accumulations. In episode II (Fig. 10h), channels are narrower, and high coherent energy is observed mostly over the slope, not constraint to the in-fills.

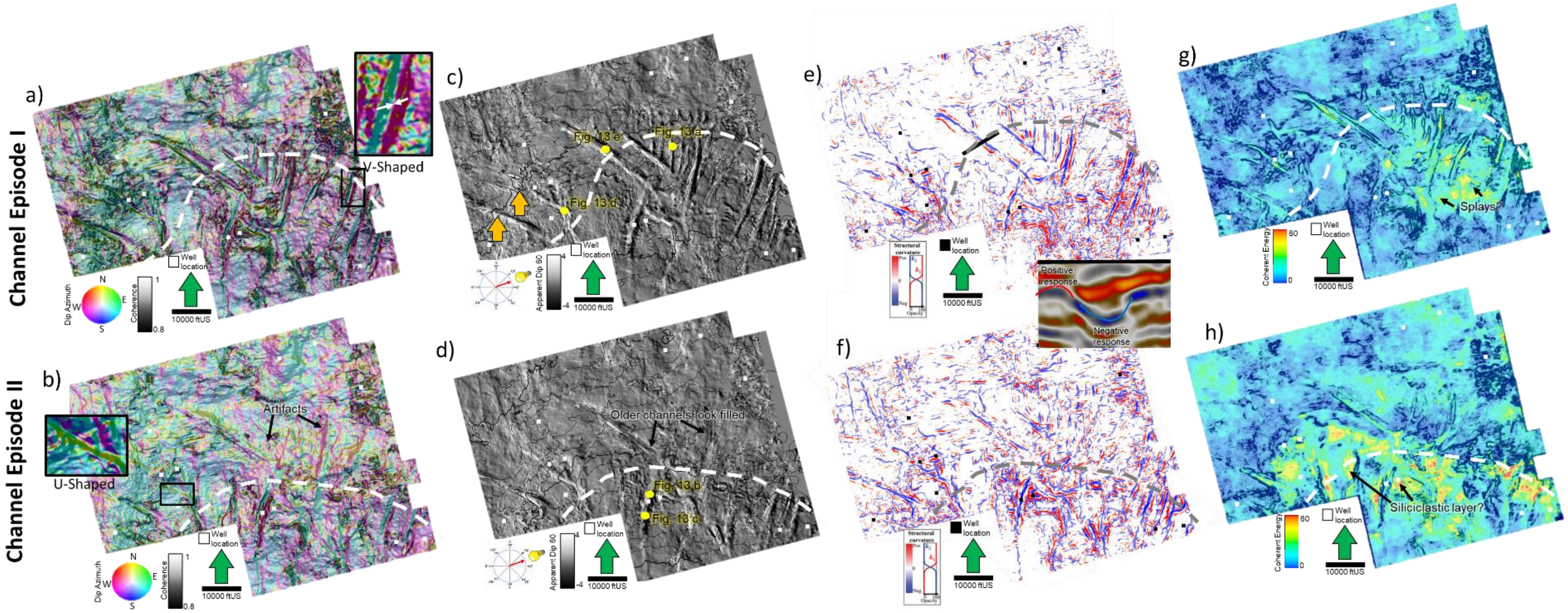
Channel Episode I
Channel Episode II
a)
V-Shaped
Dip Azimuth
N
E
S
W
Coherence
1
0.8
Well location
10000 ftUS
b)
Artifacts
U-Shaped
c)
Fig. 13.e
Fig. 13.a
Fig. 13.d
Apparent Dip 90
4
-4
d)
Older channels look filled
Fig. 13.b
Fig. 13.c
e)
Structural curvature
Pos
Neg
Opacity
Positive response
Negative response
f)
g)
Splays?
Coherent Energy
60
0
h)
Siliciclastic layer?

Figure 10. Geometric attribute extraction over the 2 channel episodes. Dashed lines denotate shelf edge interpretation. Upper figures correspond to the episode I, while lower figures are of the episode II. a) and b) dip Azimuth, dip magnitude and coherence: showing how the channel in-fills dip back and forth in an east then west alternating pattern if these are V-shaped (Zoomed shot in Fig 8a). U-shaped tend to have a constant dip (Zoomed shot in Fig 8b). c) and d) dip gradient at 60° providing a picture-like view of the channels. In episode II, older channels looked filled. e) and f) structural curvature shows the channel valleys as a negative response while overbanks are positive. g) and h) coherent energy and coherence co-rendering. High coherent energy values suggest siliciclastic channel in-fill in episode I and accumulation on the deepest part of the basin, episode II instead does not show a direct correlation to lithology, possibly associated to the much thinner channels and mixing.

Frequency attributes are employed to characterize the channel fills, whether these are homogeneous or filled in a specific pattern (e.g., gradational changes N-S, changes center to edges, etc.) as well as improving the visualization of the channels. Indirectly, this analysis intends to provide an idea of compositional changes considering the contrasting frequency response between finely intercalated (high frequency) to the thick homogeneous in fills (low frequency); assuming the in-fills are thick sandstones. The peak magnitude attribute has a similar response to the coherent energy where medium to high values are more frequent in the in-fills, this is an indication of thick and bright reflectors that could correspond to sandstones. Fig. 11a and b demonstrate this observation, although they do not seem to be entirely constrained to the interior of the channel. The peak frequency is helpful to inspect lateral changes and select optimal frequencies for the spectral decomposition analysis. Overall, the channel fill peak frequency varies from 25 to 55 Hz with a dominant value of 37 Hz (Fig. 11c, d). The small NE-SW channels (white arrows) in episode I (Fig. 11c) exhibit low values 25-27 Hz over their proximal area (north) but grade into mid to high values along the direction of deposition. This evidence the lateral variability of the mixed siliciclastic systems. Unfortunately, as discussed in the petrophysics section, the lack of well control that penetrates the channels unable making *rule of thumb* assumptions needed regarding the association of peak frequency with lithology change.

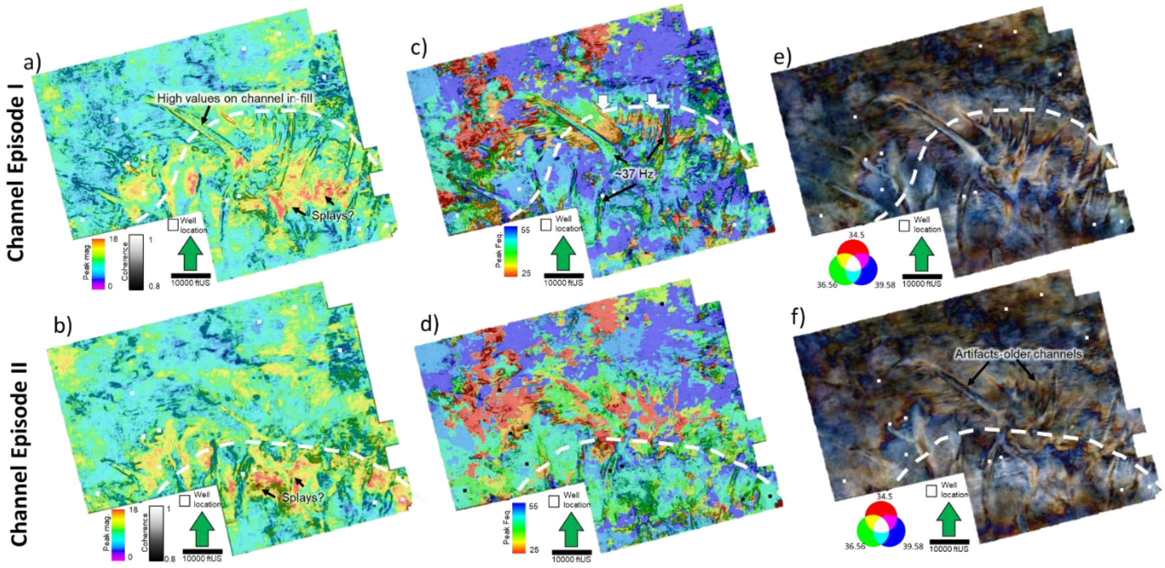

Figure 11. Frequency attribute extraction over the 2 channel episodes. Dashed lines denotate shelf edge interpretation. Upper figures correspond to the episode I, while lower figures are of the episode II. (a) Peak magnitude co-rendered with coherence (b) Peak Frequency co-rendered with coherence and C) RGB CWT spectral decomposition for the 36-39-42 frequency bands. Attribute was extracted in a 20 ms window (average time thickness of the in-fills) to show the response of the channel in-fill, not only its base.

Spectral decomposition was performed in two stages: 1) an initial (more intuitive workflow) where I selected three-frequency values based on the inspection of peak frequency maps and frequency spectrum and a second phase using the spectrogram tool to interactively select the frequencies that represent the channel fills. Modern interpretation software allows a preview of the output volumes for the interpreter to validate if it represents the feature of interest (i.e., the channel fills). In both methods, I used the continuous wavelet transform (CWT) algorithm and the best results are obtained by selecting either the dominant peak frequencies: 25-37-55 Hz or three frequencies close to the mid frequency (37 Hz): 36-39-42 (Fig. 11 e, f). The spectral decomposition matches the observations on the geometric attributes and improves the continuity of the in-fills used as input for the geobody extraction.

Amplitude-based attributes such as sweetness and amplitude curvature are also investigated and provide similar result to the coherent energy and peak magnitude attributes. High values in sweetness (deep brown colors) are mostly present in the infills, especially for episode I (Fig. 12a). This display also supports observations on Figures 11a, b where splays or unconfined deposits have a similar attribute response to the channel fills. Although, high sweetness is common in the channel interior, in episode II (Fig. 12b), I observed that channels over the basin floor (south) exhibit lower values as their frequency is smaller. Further discussion is provided in Fig. 13 where I describe how similar thickness reflectors on one same channel can present different sweetness values if their frequencies vary. Amplitude curvature display (Fig. 12c, d) is similar to the structural curvature, but instead of highlighting reflector bending, it points out bright amplitudes. As most of the channels exhibit high amplitude infills, it accurately detects the majority of them. Unlike structural curvature where the images are noisy and highlight other features besides the channels, amplitude curvature is selective and marks considerably large channels.

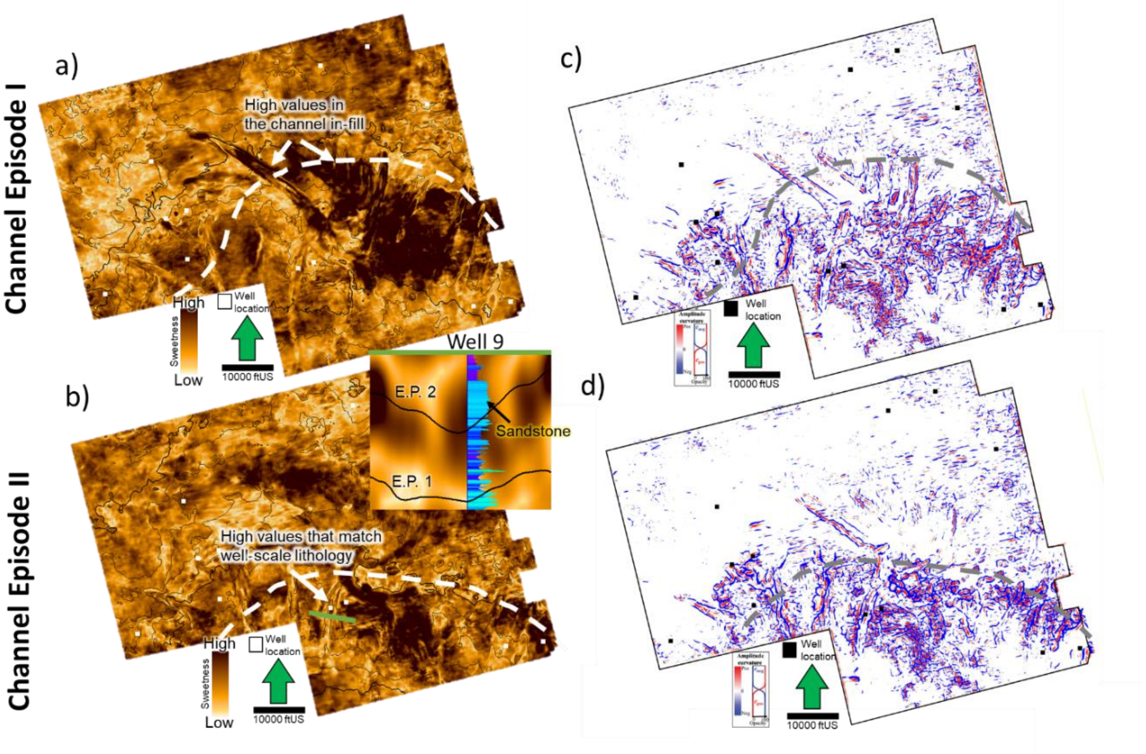

Figure 12. Amplitude accentuating attributes. Upper figures correspond to the episode I, while lower figures are of the episode II. a) and b) Sweetness. Note that channel infills have dominantly high sweetness values during episode I unlike in episode II. Frequency and amplitude decreases are the cause of the dimmer sweetness values in episode II. Figure 11 expands on these differences. c) and d) Amplitude curvature. Positive values (red) are correlated to concave features (channel fills) while negative to convex (channel edges).

Geomorphology of the submarine channel systems

In cross-sections, channels are observed as incisional troughs with high-amplitude reflections at their bottoms due to the high impedance shelf carbonates. In-fills are generally low amplitude and structureless although some of the deepest channels show the internal parallel to the base reflectors.

Geomorphological parameters such as channel sinuous length (LS1), channel straight length (LS2), sinuosity (SI), channel width (CW), channel thickness (CT), geometry (U or V) and orientation were used to describe the channel nature. Table 2 summarizes measurements of these parameters per channel event. Channel sinuosity length and straight length were measured along the minimum and maximum elongation direction between the starting and ending points of a single channel to calculate sinuosity (ratio of the two parameters). Appendix G cartoons illustrate the concepts. In this study, I use the sinuosity classification of Mueller (1968), where straight, sinuous, and meandering channels have sinuosity indexes (SI) of < 1.05, 1.05–1.5 and > 1.5, respectively. Channel width and thickness ranges were measured on the maximum values for each channel. The shape of the base proved to be very variable (Fig. 13b, c) depending on where it is relative to the shelf break is imaged. In general, I classified channels as either V-shaped or U-shaped. Channel orientation was obtained from the map view of the channels on the seismic attributes (Fig. 10 c and d) and qualitatively estimated relative to the north.

Seismic attributes stratal slices (plan view) and cross-sections allowed to image the channels in such detail to describe dimensions and morphology, also supported by conventional seismic interpretation (amplitude cross-sections). Based on their amplitude and attribute expression, I was able to identify two main categories: type I (Fig.13a, b) which extend over the steepest portion of the slope (shelf break) and are straight, deeper and have a characteristic V-shaped base while type II (Fig. 13c, d, e) are found on the low angle areas such as either the outer shelf or in the basin floor and tend to be slightly more sinuous, shallow and U-shaped. Overall, channels are mostly straight with a sinuosity index 1-1.07 and a width range of 600-1700 ft (180-500 m). Channel thickness was assessed thought the inspection of the depth converted seismic volume and the well penetrations ranging from 50-200 ft (15-60 m). An interesting feature observed in the channels is the presence of the multiples below the incisions which are interpreted as *push-down* artifacts due to the impedance differences between the in-fill (sandstone) and the shelf (tight limestone) (Dyment & Bano, 1991), which could be mistakenly related to aggradation. Both types of channels were interpreted as erosional and single story due to this lack of lateral migration. This will be further debated in the discussion section. Seismic attribute cross-sections also helped to infer that type I channels in fills tend to have slightly brighter amplitude than their type II counterparts, resulting in a dimmer response in sweetness and peak magnitude as depicted in Fig 13c.

Another morphological difference was the infill reflector pattern. Type I infills mimic the base of the channel, being mostly V-shaped; while type II are quite variable: changing from near flat to shingled.

Table 2. Main types of channel morphologies as observed in the studied interval. The description and the parameters include channel width (CW), sinuosity, thickness, type of base (U or V), orientation, and episode. Appendix G serves as an explanation for the parameters. Modified from Niyazi et al. (2018). Channels were classified based on their dominant character, considering that some evolve from type I into type II.

Channel	Channel type	Number of channels	Incision type (V or U)	sinuosity	Degree of sinuosity	channel width (ft)	channel thickness (ft)
Episode I	type I	14	V	1.01-1.05	straight	600-1700	200-50
	Type II	2	U	1.05-1.07	low sinuosity	900-1300	100-50
Episode II	type I	3	V	1.01-1.05	straight	600-1500	150-50

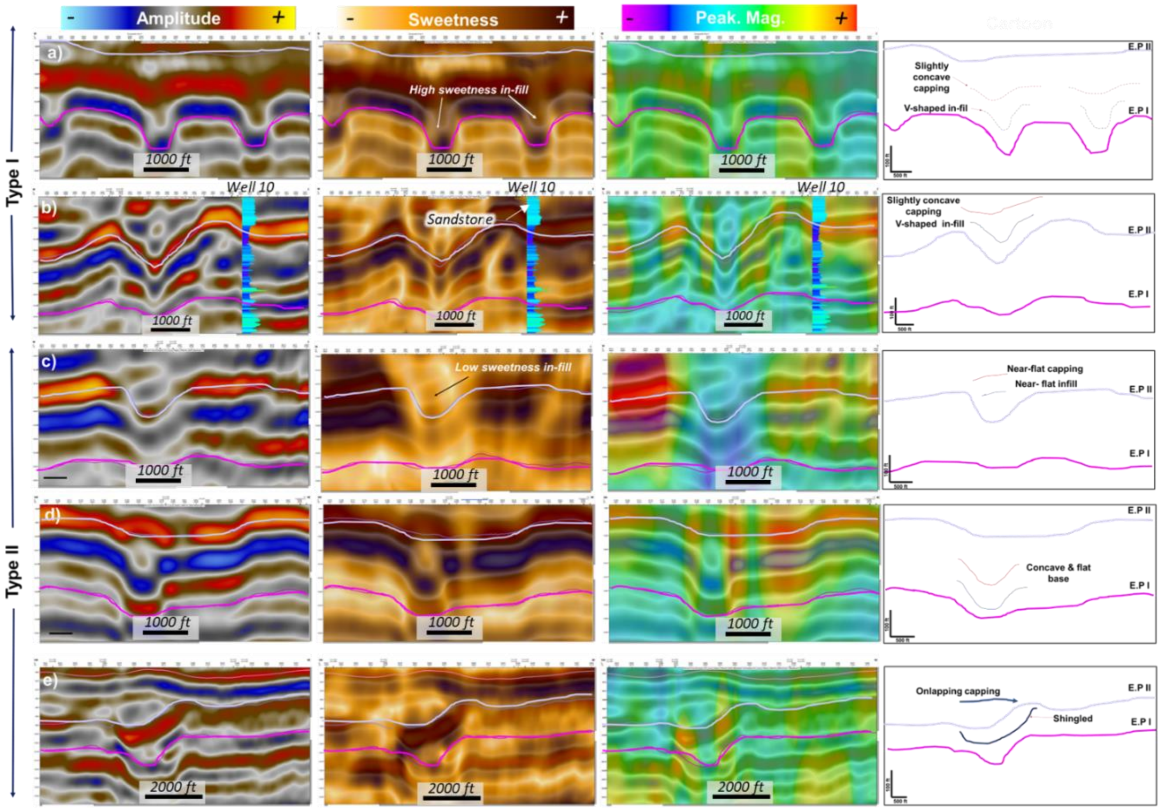

Figure 13. Seismic section showing (from left to right) the amplitude section, peak magnitude and sweetness attribute response and a cartoon of the interpretation of channel-fill styles. Location of the examples can be found on Fig. 10c, and 10d. Type I channels are slightly more sinuous and shallower compared to type II. Both types of channels are present during the two episodes and longer channels show an evolution from type II to type I. Erosive power decreases from north to south as the slope angle decreases as well. Overall, I noticed that the attribute response is not very consistent for the channel infills. As seen in the map view, high sweetness and high peak magnitude values tend to be constraint to the in-fills but varies along the strike of the channel. For example, the channel on Fig. 13 b and c has a high sweetness and peak magnitude value b) but changes into very low values c). This could be associated with changes in bed thickness, composition or petrophysical properties (e.g., porosity).

Geobodies and facies modeling

Using the spectral decomposition RGB blending, I cross-plotted the three selected frequencies (either 25-37-55 Hz or 36-39-42 Hz) and using the dynamic sample selection over a horizon slice, I choose samples over the channel fills and extracted geobodies by simultaneously selecting samples in the cross-plot that, according to the interpreter, represents exclusively the infills (Fig. 14). Spectral components were selected in the time domain and then converted to the depth, following the conventional workflow (Murat Alyaz, 2022). The output is also vertically constrained to a depth range (top and bottom horizons) selected upon the interpreter's selection. This process is repeated until the output accurately embodies the observations of the interpreter. Often, post-generation editing was required to merge or delete geobodies that were excluded of the desired result. A total of nineteen geobodies are then upscaled to the model grid to be later overwritten as sandstone in the facies model.

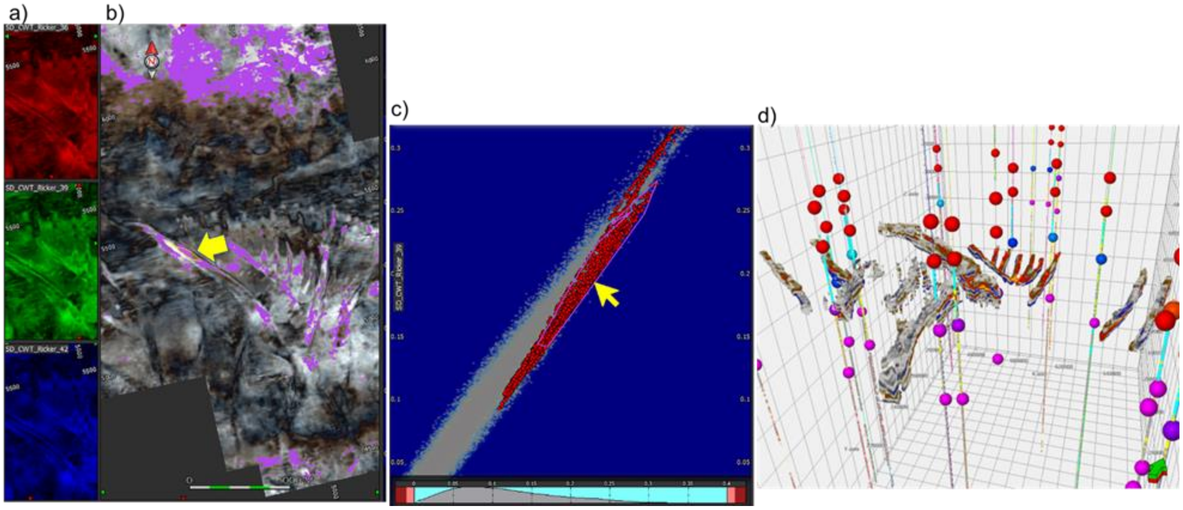

Figure 14. Channel geobodies extraction. a) Individual spectral component (36-39-42 Hz) horizon slice. b) RGB co-render over the channel episode I c) cross plot of the 3 main frequencies in the depth domain. Yellow arrows are highlight the polygons chose for geobody generation. d) 3D view of the 19 channel geobodies used in the modeling area.

Post-stack inversion and facies probability maps

The inversion result that showed the best results was the one from the top of the LSA to the Queen with 5 interactions and using a statistical wavelet with no phase rotation. Average correlation is ~95% with error ranging from 20 to 40% (Appendix Ha, b). However, additional work could be done to further fine tune the inversion parameters.

Cross plots of AI versus inverted AI were also performed to explore more localized discrepancies as well as qualitative checked at the well sites as depicted on appendix Hc,d. Overall, the acoustic impedance inversion volume identifies the lateral and vertical variability, but some zones are inconsistent (e.g., Well 1 upper zones (A-D) have relatively high AI values >40000 (ft*s)(g*cc), but the inverted volume has lower values; this results in depicting dolostones as limestones for this section, as will be discussed later due to the heterogeneity and shortage of well control).

Using the workflow in Fig. 4, the proportional (used here as probability) maps (Appendix I) show that zones A to C where progradation is not evident, limestone is widespread across the area with considerable accumulations over the western side, decreasing considerably towards the northwest corner where dolomite and sandstones are predominant. Zones D to H are characterized by significant progradation north to south and the probability maps reflect this migration. Limestone seems to be restrained to the slope and the proximal area, especially towards the west, while dolostone is scattered throughout the dataset but mostly present in the northeast. Sandstones are generally associated with low acoustic impedance values and tend to be constrained to the channel infills (linear features over the slope) and to the basin floor splay-like accumulations. Zone I represents the Lower San Andres and as shown on Fig. 2b is composed of sandstones and shales with minor limestone and dolostone to the east (Appendix Ii).

3D facies model

The stratigraphic framework of the model is composed of nine zones that represent the geometries observed on seismic (Fig. 15a, b). For the rock-type model, for all rock types, vertical variograms were set based on their variability (Appendix D), while horizontal were mostly driven by the probabilistic maps calculated for each zone from inversion (Fig. 15c, Appendix I, Appendix J). Sandstone occurrence in Zones E and F is limited to the channel geobodies location, therefore overwritten into the 3D facies model.

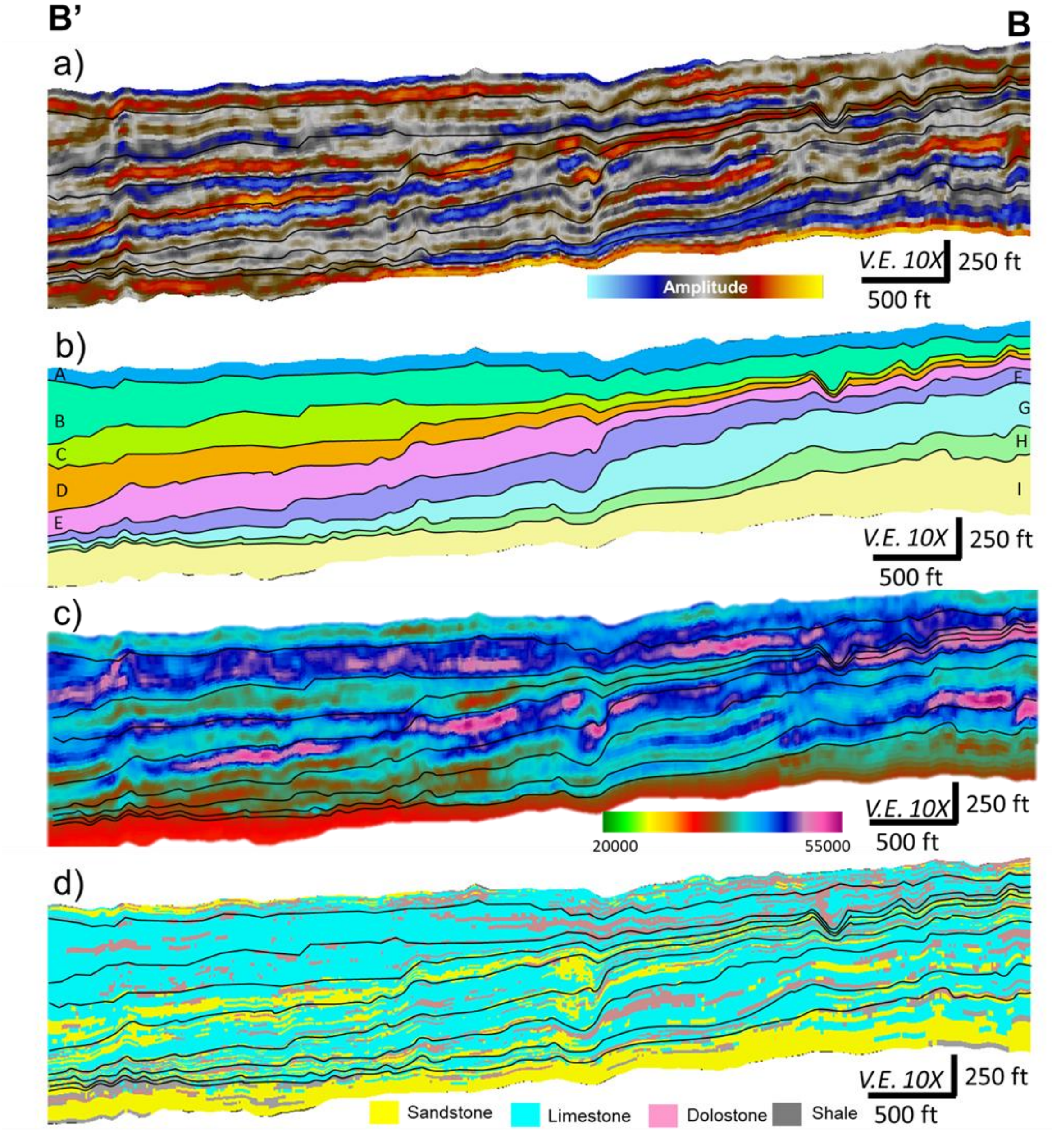

Figure 15. North-south cross section. B’-B section is denotated on Fig. 5a. a) Upscaled seismic showing the reflector configuration (clinoforms and horizons selected), b) stratigraphic zones illustrating the thickness variations along the progradation direction

(clinoforms), c) P-impedance cross-section showing the lateral and horizontal variability and d) Spatial distribution of rock types modeled using the proportion maps per zone based on P-impedance (Appendix I--limestone maps). Zone A-C are carbonate rich with dolomite mostly present over the proximal area (north) and limestone towards the distal area. Zones D-H where progradation is evident limestone is restricted to the shelf with minor proportion of dolomite in the north and significant sandstone accumulation in the shelf as well and in the distal portion. Zone I instead is sandstone and shale rich with minor limestone and dolostone.

Each stratigraphic zone has a dominant mineralogy and rock-type composition (Fig. 15d) that follows the spatial distribution of the rock type probability maps (Appendix I & J), e.g., Zone A-C are characterized by dolostones intercalated with limestone (mostly to the west) and sandstones to the east. Zones D-F are composed of sandstones and limestone. Note in the along dip section that sandstone is mostly encountered in the "slope" or the steepest part of the clinoform or deeper in the basin, while in the shelf, limestone is more common. These zones are also expected to have a considerable amount of sand as the channel episodes occurred in this interval. Zones G-I are again an intercalation of the three rock types with a noticeable base of sandstone as it covers the top part of the LSA.

In summary, the Lower San Andres is characterized by sandstones and shales. Upper San Andres is composed by a mixture of sandstones and dolostones that grade into limestones. Lithology intercalation is more frequently seen in the basin-ward area (Wells 9, 10 and 11). Moving stratigraphically upward through the Grayburg, sandstones are frequently found related to the channel incisions in the basin area (south) (Fig. 15d, zones F, G; Fig. 16), although towards the north-west (close to the CBP) sandstone accumulations are minimal, being limestones the dominant rock type (Fig. 16). The Middle Grayburg is dominantly limestone and grade into dolostone intercalated with sandstones or siltstones in the Upper Grayburg (Zone D to A). As discussed in the petrophysics results, presence of evaporites (anhydrite) in the Upper Grayburg is common, which is not pictured here, due to well log shortage on this interval.

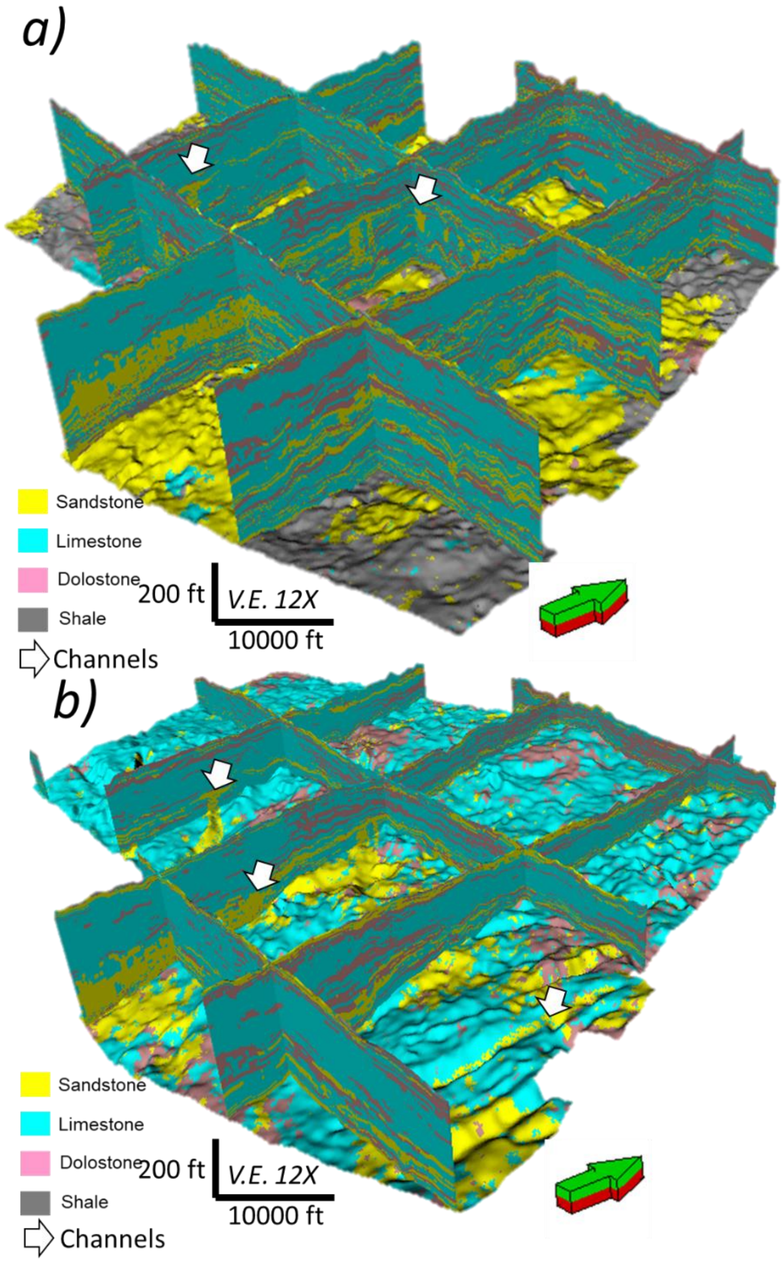

Figure 16. 3D view of the facies model. a) Complete vertical view bounded in the bottom by the base of the model. Note that the limestone and dolostone and intercalated throughout the section dolostone to limestone ratio increases towards the east in the upper zones (A-D). b) Zones A-E emphasize the channelized interval (zone E). Channels are pointed with white arrows.

Discussion

Challenges on the interpretation of mixed carbonate-siliciclastic systems

Interpretation of mixed systems comprises multiple challenges due to the variability in rock physics, which affects the impedance response of the post stack volume. One of the artifacts encountered is the pull-down effect below the channel incisions. This is a common pitfall in carbonate systems as time-migrated data will suffer from lateral changes in apparent structure due to overlying lateral changes in velocity. Push down occurs when lower velocity anomalies such as incised channels or shallow gas are located on top of high velocity facies (carbonate platform, in this case), producing a concave up semicircular *shadow* that mimics the channel base expression (Dyment & Bano, 1991; Marfurt & Alves, 2015, Harishidayat & Raja, 2022). For the channels with well penetrations, I overcame this uncertainty by defining the base of the channels to where thick sandstone accumulation is observed.

As shown at the well-log sections and facies model, lateral and vertical lithology variability in both the San Andres and Grayburg formations require an effective estimation that not only separates carbonate versus siliciclastic, but also discriminates between dolostone and limestone as ρmaa-Umaa. However, unlike in other studies (Dingmore, 2020; Pranter et al., 2004) where the lithology has intrinsic reservoir properties (porosity), limestones and dolostones are quite variable as reflected in the acoustic impedance (seismic scale) due to changes in the porosity and mineral ratios (i.e., Fig. 8 shows how even when a sample is classified as sandstone it can contain considerable proportions of calcite and dolomite, altering the rock properties including acoustic impedance). Porosity ranges from ~6-26% for the dolostones and ~1-26% for the limestones. This variability and overlap in the acoustic impedance response makes the distinction between these two facies difficult at a seismic scale and supports the lack of consistency in the attribute response for the same facies. Similarly, to the carbonates, sandstone porosity ranges from 2-16% (Appendix Ba). For all the lithologies, cementation, brecciation, dissolution, anhydrite alteration and removal among other diagenetic processes affect the porosity and consequently reservoir quality (Ruppel & Lucia, 1996; Ojeda, 2011). This variability was also described at the core scale (well 1) where, for instance, limestones are both tight and porous depending on the dissolution degree of the fusulinids or biogenetic material (Fig. 6). Although the attribute response was not consistent in tracking the compositional changes, it provided insights on the interpretation of the channel evolution not observed in the amplitude analysis.

Channel morphology and analog comparison

Verma et al. (2023) identified five major channelized events in the Grayburg and San Andres formations. I focused on two of these episodes developed during the clinoform progradation of the Upper San Andres (episode I) and Lower Grayburg (episode II) over the south area of the seismic survey.

In general, channelized features are consistently oriented slightly north-west to south-east (nearly N-S) following the direction of progradation and the structure of the basin (Table 3). As mentioned, the area of study is located in between the Central Basin Platform (CBP) to the west and the Midland Basin to the east. As such, some of the channels seem to descend from the west (CBP) due to its relief (orange arrows, Fig. 10c). Additionally, subtle faulting/folding is attributed to the channel azimuth trends (Verma et al., 2022) as this matches the fault orientations in the Woodford to Base of San Andres levels at the area of study (Verma & Scipione, 2020). Faulting that follows this orientation have been reported in the overlying Yates Formation, which was attributed to fault reactivation (Gray et al., 2022).

The differences in the base type U vs V are mostly related to the erosive power and the angle of the slope in which the channel is incising. As shown on Fig.13b cross-sections in the proximal area (north) exhibit a V-shaped base that evolves into a U-shape further into the basin (Fig.13c), suggesting that V-shaped are more erosive than the U-shaped (Niyazi et al., 2018). However, both channel types are presumably erosional due to lack of aggradational features (vertical and horizontal).

Comparison to world-wide and Permian Basin ancient analogs (Natih Formation in Oman, Cherry Canyon in the Delaware Basin) (Droste, 2010; McHargue et al., 2011) shows similar geomorphological features. These analogs are also relatively narrow (<3300 ft; 1000m) and shallow ~100 ft (30 m) deep. Depositional mechanisms (discussed in following sections) are also similar, mainly developed during sea level drops (LST) or during high stands system tracts where sediment accumulation triggers erosive channels or mass transport deposits.

Comparison to channel systems in the Delaware Basin

The Delaware Basin siliciclastic members have been studied extensively at outcrop scale and channel systems are more complex compared to the Midland Basin. Evolution of submarine channels usually begins with the development of low sinuosity incisions by erosion and ends with the migration of leveed channels (Deptuck et al., 2007; Mayall et al., 2006; McHargue et al., 2011). In the Delaware Basin, multiple stages of incision and channel-levee systems identification contrast with the erosional channels described in the area of study as the system is more mature. Widths range from approximately 980-2600 ft (300 to 800 m) (Phelps & Kerans, 2007) which are considerably wider than these channelized features 600-1700 ft (150-500 m) (Table 2). Another major difference is related to the lithologies, in the Delaware basin channel levees are composed of carbonate debrites and mud while their Midland Basin analogs are presumably sandstone rich. Differences between these channel systems relate to the availability of fine-grained sediments.

Channel in-fill deposition: build-cut-fill-spill model

A depositional model that suits this channel system is *build-cut-fill-spill*, which divides the deposition in four stages, and it is used to explain the stratigraphy of the Brushy Canyon (analog of the Guadalupian Channels in the Midland Basin) (Gardner et al., 2000, 2003). In stage 1 (*build*), there is deposition of unconfined flows bypassing high gradient profile positions. This is followed by an erosive phase (*cut*) where sediment bypasses to low-gradient profile positions provoking the collapse of sediment banks. During the fill stage, the main phase of channel deposition occurs, and materials could be siliciclastic, carbonates or a mixture of both. Finally, after the channels are filled, deposition continues and either the channel is abandoned or re-initiated as multiple *cut-fill-spill* deposits. Fig. 17 summarizes in a cartoon the four stages for the channels in the area of interest. Unlike in the Brushy Canyon example, lack of mud supply prevented levee development and therefore building stage is mostly carbonate debritic progradation.

This model is widely accepted and matches the observations on seismic as the channels are mostly developed over the slope where the sediment accumulation and slope angle promote erosion. Amplitude and attribute cross-sections with overlaid well logs (GR), indicate that channels are originally incised in a carbonate platform (*build* and *cut*), then filled with clastics (*fill*) and finally capped by carbonates (*spill*) (Fig. 13b). Due to the shortage of channel-penetrating well control, I assumed the channel are siliciclastic/sandstone filled as suggested by wells 9 and 10 that penetrate some of the southern (basin) channels. As the 3D lithology model and cross-sections showed, siliciclastic infills are more dominant on the deepest part of the basin since channels are deeper and sediment supply is more likely to be siliciclastic as it is moving away from the carbonate build-ups at north-west (CBP) (Fig.16). Quartz-rich sandstone channels have been reported as well in the Midland Basin cutting the carbonate progradation and interpreted as tidal channels (Todd, 1976).

A key question to understand the lithology variability is the origin of the siliciclastic components in this carbonate-rich basin. No provenance studies of the Midland Basin sandstones are available but similar mechanisms to the Brushy and Cherry Canyon units are inferred. For these units' sediment source are the structural highs that surround the Midland Basin (Northwest Shelf) (Broadhead & Justman, 2000). For the Delaware Basin case, siliciclastics were probably originated from granitic rock in the ancestral Front Range in Colorado, given the high feldspar content of siliciclastic facies (Basham, 1996). No petrographic studies are available of the channel sandstones in the Midland Basin, but relatively high gamma ray response could be associated with the feldspar content described in the Delaware Basin. Eolian sandstone origin has also been widely discussed and supported by the match in the prevailing wind directions with the orientations of the sub-marine channel systems. During the Guadalupian, eolian sandstones were deposited northeasterly, northerly, or northwesterly (present azimuths) based on crossbedding measurement in the southwestern USA (Peterson, 1988). Further provenance studies are required to determine if as in the Delaware Basin, the Northwest shelf acts as unique sediment source or if alternatives such as the Central Basin Platform itself provided carbonate material that filled out the channels. Regardless of the source location, episodic siliciclastic deposition is controlled mostly by changes in the sea level.

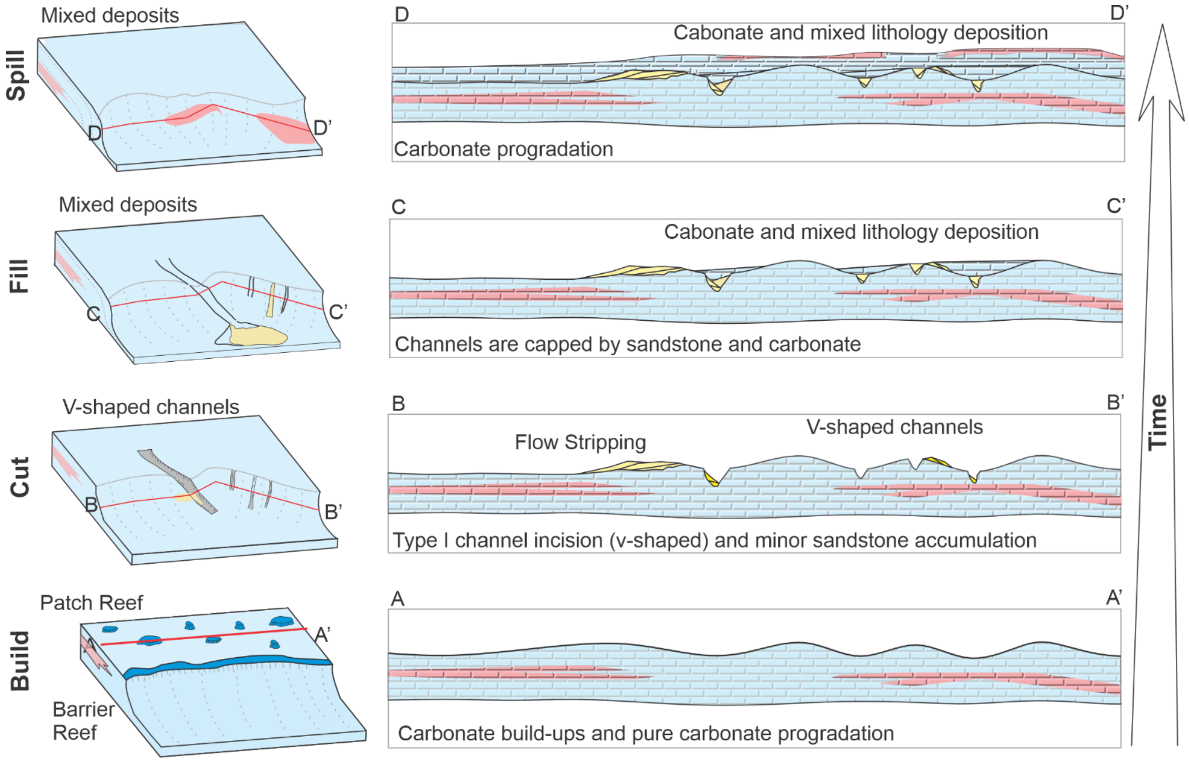

Figure 17. Four temporal and spatial domains, *build, cut, fill, spill* (BCFS), characterize the principal phases of submarine channel deposition. These domains relate variable confinement to the probable facies recording deposition from a region within a series of related flows and their contribution to channel, wedge and lobe sedimentary bodies. This diagram shows the BCFS phases through the evolution of a single-story channel. Modified from Gardner et al (2003).

Depositional controls: Sequence stratigraphy

The San Andres and Grayburg deposition are explained by the reciprocal sedimentation model, in which cyclical deposition alternating shelf-centered shallow-water carbonates and basin-centered terrigenous siliciclastics occur (Van Siclen, 1958; Silver & Todd, 1969; Meissner, 1969, 1972). Terrigenous sands (most likely eolian) are transported into the basin during lowstands of relative sea level, whereas shallow-water carbonates are deposited on the shelf during relatively high sea level when broad back reef lagoons prevented the terrigenous sediments from reaching the basin. The analogs of the San Andres–Grayburg strata, the Brushy Canyon and Cherry Canyon formations of the Delaware Mountain Group mark distinct lowstand events (King, 1942; Harms & Pray, 1974) of bypass of eolian sandstone and siltstone. Channels identified in the Upper San Andres were originated during the G-9 high stand system tract (Fig. 2a), which in the classic model would produce carbonate buildups, but instead multiple gully-like incisions were found. This is explained by limited accommodation space during the G-9 HST allowed generation of only erosional turbidites progradational clinoforms (Sonnenfeld & Cross, 1993).

Limited accommodation space is related to the intense north to south progradation/sediment accumulation observed in the horizon mapping (Fig. 9). Shelf margin movement, marked by the depocenter movement and channel development, suggests shrinkage of the Midland Basin during the Guadalupian series (Ward & Trentham, 2020) (Fig. 18).

Similarly, Gardner (1992) and Nance (2006) explain for the Brushy Canyon Formation in the Delaware Basin that during highstands processes such as restriction of continental siliciclastic depositional environments well shelfward of shelf margin, deposition in basin of windblown silt, and gravity transport of shelf-margin carbonate debris are common. Meanwhile, lowstands are characterized by encroachment of prominently eolian depositional environments on shelf margin, accumulation of siliciclastics on upper slope, slumping of accumulated siliciclastics, and downslope transport of siliciclastics by turbidity flow. These observations match my interpretation as the during highstands sediment accumulation and bypass (gullies development) is typical to later be filled by sandstone-rich turbidity flows in the lowstands.

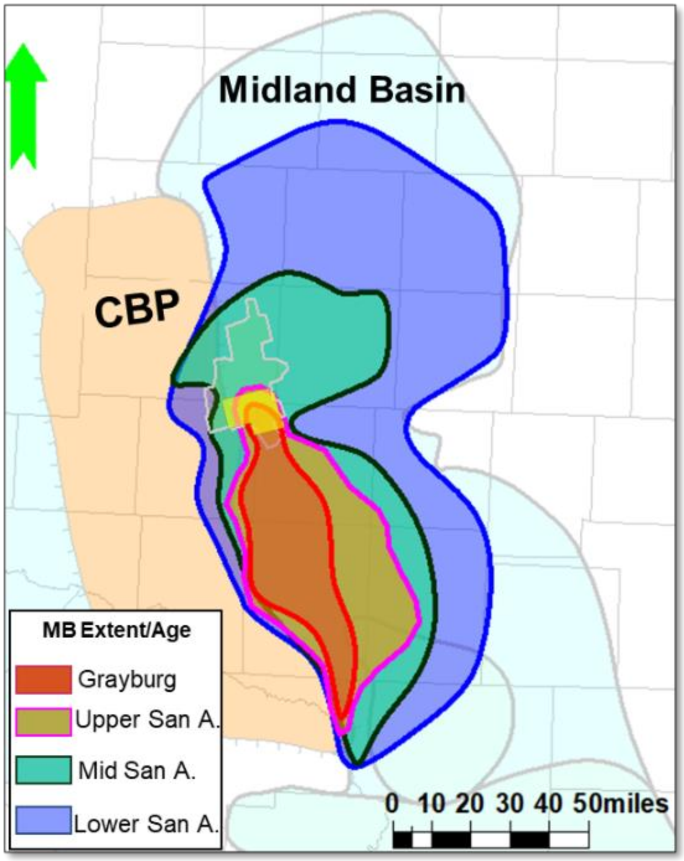

Figure 18. Map of the extension of the Midland Basin during the Guadalupian time showing correlation between the closure of the basin and progradation maps of this study. Modified from Ward & Trentham (2020).

Conclusions

I presented an innovative integrated study of the mixed clastic–carbonate strata of the San Andres–Grayburg (G-8 to G-12 HFS) in the Midland Basin. A channelized system was identified and characterized in this interval at core, well log and seismic scales. Cores and well-logs demonstrated that at a fine scale, the lithological heterogeneity is related to the change in the mineral proportions (quartz, dolomite and limestone) and the petrophysical properties (porosity, permeability). Seismic attributes and impedance analysis also supported the complexity of the system showing the morphology of the channels and the heterogeneity in the in-fills.

Geomorphology analysis showed that two main episodes of channel incision occurred in the AOS. For both, two types of channels are identified: type I and type II, characterized by straight, V-shaped and incised and slightly more sinuous, U-shaped and shallower features, respectively. Both channel types are erosive, and their deposition is explained by the single-story *build-cut-fill-spill* (BCFS) channel model.

In conjunction with the seismic geomorphology results and the petrophysical interpretations, I concluded that channel fills are dominantly siliciclastic and contrast with the carbonate platform in which the channels incise. I depict this on the 3D facies model that also reflects the dolomite and limestone variability. Limestones were more frequently described in the Upper San Andres and Lower Grayburg, especially in the western part of the modeled area, which is proximal to the CBP, one of the presumable sediment sources. Dolostones instead are found intercalated with sandstones in the Upper Grayburg and capping the Grayburg Formation. Overall, these results match the sequence stratigraphic framework where a sea level drop also enhanced by the shrinkage of the Midland Basin yield to the deposition of shallow/environment lithologies.

References

Asmus J. A. & Grammar, G. M.. (2013). Characterization of deep-water carbonate turbidites and mass-transport deposits utilizing high-resolution electrical borehole image logs: Upper Leonardian (lower Permian) Upper Bone Spring Limestone, Delaware Basin, Southeast New Mexico and West Texas. *Gulf Coast Association of Geological Societies Transactions, 63,* 27–65.

Asquith, G.B. & Gibson, C.R. (1982). Basic Well Log Analysis for Geologists. The

American Association of Petroleum Geologists (AAPG), Tulsa, OK.

Barnaby, R. J., & Ward, W. B. (2007). Outcrop analog for mixed siliciclastic-carbonate ramp reservoirs - Stratigraphic hierarchy, facies architecture, and geologic heterogeneity: Grayburg Formation, Permian Basin, U.S.A. *Journal of Sedimentary Research*, *77*(1–2), 34–58. https://doi.org/10.2110/jsr.2007.007

Basham, W. L. (1996). Delaware Mountain Group sandstone channel orientations: implications for sediment source and deposition, in DeMis, W. D., and Cole, A. G., eds., The Brushy Canyon play in outcrop and subsurface: concepts and examples. *Society of Economic Paleontologists and Mineralogists Permian Basin Section Publication 96-38*, 91–102.

Bhatnagar, P., Verma, S., & Bianco, R. (2019). Characterization of mass transport deposits using seismic attributes: Upper Leonard Formation, Permian Basin. *Interpretation*, *7*(4), SK19–SK32. https://doi.org/10.1190/INT-2019-0036.1

Broadhead, R. F., & Justman, H. A. (2000). Regional controls on oil accumulations, lower Brushy Canyon Formation, southeast New Mexico, in DeMis, W. D., Nelis, M. K., and Trentham, R. C., eds., The Permian Basin: proving ground for tomorrow's technologies. *West Texas Geological Society Publication 00*-109, 9–18.

Caf, A. (2022). Quantitative Seismic Interpretation and Machine Learning Applications for Subsurface Characterization and Modeling. University of Oklahoma.

Chiarella, D. & Longhitano, S.G. (2012). Distinguishing depositional environments in shallow-water mixed, bio-siliciclastic deposits on the basis of the degree of heterolithic segregation (Gelasian, southern Italy). *Journal of Sedimentary Research*, *82*, 969–990.

https://doi.org/10.2110/jsr.2012.78.

Chiarella, D., S. G. Longhitano, & Tropeano, M. (2017). Types of mixing and heterogeneities in siliciclastic-carbonate sediments. *Marine and Petroleum Geology, 88*, 617–627. https://doi.org/10.1016/J.MARPETGEO.2017.09.010

Chopra, S. & Marfurt, K.J. (2007). Overview of Seismic Attributes. In: Seismic Attributes for Prospect Identification and Reservoir Characterization. 1–24.

Chopra, S., & Marfurt, K. J. (2013). Structural curvature versus amplitude curvature. *The Leading Edge, 32*(2), 178–184. https://doi.org/10.1190/tle32020178.1

Chopra, S., & Marfurt, K.J. (2016). Spectral decomposition and spectral balancing of seismic data. *The Leading Edge, 35*, 176–179. https://doi.org/10.1190/tle35020176.1

Cluff, R., Cluff, S., Sharma, R., & Sutton, C. (2015). A Deterministic Lithology Model for the Green River-Upper Wasatch Interval of the Uinta Basin. *AAPG Annual Convention & Exhibition 2015*.

Deptuck, M. E., Sylvester, Z., Pirmez, C., & O'Byrne, C. (2007). Migration-aggradation history and 3-D seismic geomorphology of submarine channels in the Pleistocene Benin-major Canyon, western Niger Delta slope. *Marine and Petroleum Geology, 24*(6–9), 406–433. https://doi.org/10.1016/j.marpetgeo.2007.01.005

Dingmore, L. (2020). Stratigraphic variability of mineralogy, rock types, and porosity of the Wolfcamp Formation using multi-mineral petrophysical analysis and seismically constrained reservoir modeling, Norwest Shelf, Delaware Basin. University of Oklahoma.

Dolton, G.L., Coury, A.B., Frezon, S.E., Robinson, K., Varnes, K.L., Wunder, J.M., & Allen, R.W. (1979). Estimates of undiscovered oil and gas, Permian Basin, west Texas and southeast New Mexico. *U. S. Geological Survey Open-file Report* 79-838, 118 p.

Doveton, J. H. (1994). Numerical Methods for Mineral Estimation from Well Logs, AAPG Datapages/Archives, Special Publications of SEPM, 123-133.

Droste, H. (2010). High-resolution seismic stratigraphy of the Shu'aiba and Natih formations in the Sultanate of Oman: Implications for Cretaceous epeiric carbonate platform systems. *Geological Society of London, Special Publication, 329*, 145–162. https://doi.org/10.1144/SP329.7

Dutton, S. P., E. M. Kim, R. F. Broadhead, C. L. Breton, W. D. Raatz, S. C. Ruppel, & Kerans, C.. (2005a). Play analysis and digital portfolio of major oil reservoirs in the Permian Basin: Application and transfer of advanced geological and engineering technologies for incremental production opportunities: Austin, Texas, Bureau of Economic Geology, The University of Texas at Austin. *Report of Investigations 271*, 302 p.

Dutton, S. P., E. M. Kim, R. F. Broadhead, W. D. Raatz, C. L. Breton, S. C. Ruppel, & Kerans C. (2005b). Play analysis and leading-edge oil-reservoir development methods in the Permian Basin: Increased recovery through advanced technologies. *AAPG Bulletin, 89*(5), 553–576. doi:10.1306/12070404093.

EIA (US Energy Information administration). (2022). Advances in technology led to record new well productivity in the Permian Basin in 2021.Entzminger, D. J., K. Ferdinand, D. Lawson, B. Loucks, P. Mescher, & Patty, K. (2000). Corrigan-Cowden— Breathing new life into an old waterflood: The Permian basin: Proving ground for tomorrow's technologies: Midland, Texas. *West Texas Geological Society Publication* 00-109, p. 75.

Ewing, T. E. (1991). The tectonic framework of Texas. Bureau of Economic Geology, The University of Texas at Austin, 36 p.

Farfour, M., Yoon, W. & Kim, J. (2015). Seismic attributes and acoustic impedance inversion in interpretation of complex hydrocarbon reservoirs. *Journal of Applied Geophysics, 114*, 68-80. https://doi.org/10.1016/j.jappgeo.2015.01.008

Fitchen, W. M., Gardner, M. H., Kerans, C., Sonnenfeld, M. D., Tinker, S. & Wardlaw, N. L. (1992) Evolution of platform and basin architecture in mixed carbonate-siliciclastic sequences latest Leonardian through Guadalupian, Delaware Basin. *American Association of Petroleum Geologists Annual Convention*, p. 41.

Friedman, G. M., Ghosh, S. K., & Urschel, S. (1990). Petrophysical characteristics related to depositional environments and diagenetic overprint: a case study of the San Andres Formation, Mabee field, west Texas, in Bebout, D. G. and Harris,P. M., eds., Geologic and engineering approaches in evaluation of San Andres/Grayburg hydrocarbon reservoirs—Permian Basin. The University of Texas at Austin, Bureau of Economic Geology Publication, 125–144.

Garcia-Hidalgo, J. F., Gil, J., Segura, M., & Domínguez, C. (2007). Internal anatomy of a mixed siliciclastic–carbonate platform: the Late Cenomanian–Mid Turonian at the southern margin of the Spanish Central System. *Sedimentology, 54*(6), 1245–1271. doi:10.1111/j.1365-3091.2007.00880.x

Gardiner, W. B. (1990). Fault fabric and structural subprovinces of the Central basin Platform: A model for strike—slip movement, in Flis, J. E., and Price, R. C., eds., Permian basin Oil and Gas Fields: Innovative Ideas in Exploration and Development: Midland. *West Texas Geological Society*, 90–87, 15–27.

Gardner, M. H. (1992). Sequence stratigraphy of eolian-derived turbidites; deep water sedimentation patterns along an arid carbonate platform and their impact on hydrocarbon recovery in Delaware Mountain Group reservoirs, West Texas, in Mruk, D. H., and Curran, B. C., eds., Permian Basin exploration and production strategies; applications of sequence stratigraphic and reservoir characterization concepts. *West Texas Geological Society Publication*, 92-91, 7–11

Gardner, M. H., & Borer, J. M. (2000). Submarine Channel Architecture along a Slope to Basin Profile, Permian Brushy Canyon Formation, West Texas (68). In: Fine-Grained Turbidite Systems. *AAPG Memoir 72/SEPM Special Publication*, 195–215.

Gardner, M. H., Borer, J. M., Melick, J. J., Mavilla, N., Dechesne, M., & Wagerle, R. N. (2003). Stratigraphic process-response model for submarine channels and related features from studies of Permian Brushy Canyon outcrops, West Texas. *Marine and Petroleum Geology, 20*(6–8), 757–787. https://doi.org/10.1016/j.marpetgeo.2003.07.004

Gray, J., A. Wilkins, & Verma, S. (2022). Permian Basin Trend Analysis Using Seismic Attribute. *5th Geoscience Symposium at University of Texas at Permian Basin*.

Guo, L., Yang, L., Cai, L., & Zheng, Z.. (2018). Structure-oriented filtering for seismic images using nonlocal median filter. *SEG Technical Program Expanded Abstracts*, 4623-4627. https://doi.org/10.1190/segam2018-2998154.1

Harishidayat, D., & Raja, W. R. (2022). Quantitative Seismic Geomorphology of Four Different Types of the Continental Slope Channel Complexes in the Canterbury Basin, New Zealand. *Applied Sciences (Switzerland), 12*(9). https://doi.org/10.3390/app12094386

Hart, B. S. (2008). Channel detection in 3-D seismic data using sweetness. *AAPG Bulletin, 92*(6), 733-742. https://doi.org/10.1306/02050807127

He, Y., Kerans, C., Zeng, H., Janson, X., & Scott, S. Z. (2019). Improving three-dimensional high-order seismic-stratigraphic interpretation for reservoir model construction: An example of geostatistical and seismic forward modeling of Permian San Andres shelf-Grayburg platform mixed clastic-carbonate strata. *AAPG Bulletin,103*(8), 1839-1887. https://doi.org/10.1306/11211817244

Hills, J. (1984). Sedimentation, Tectonism, and Hydrocarbon Generation in Delaware Basin, West Texas and Southeastern New Mexico. *AAPG Bulletin, 68*, 250-267. https://doi.org/10.1306/AD460A08-16F7-11D7-8645000102C1865D

Hills, J. M. (1985). Structural evolution of the Permian basin of west Texas and New Mexico, in Dickerson, P. W., and Muehlberger, W. R., eds., Structure and Tectonics of Trans-Pecos Texas: Midland. *West Texas Geological Society*, 85–81, 89–99.

Harms, J.C. & Pray, L.C.. (1974). Erosion and deposition along the mid-Permian intracratonic basin margin, Guadalupe Mountains, Texas. R.H. Dott Jr., R.H. Shaver (Eds.), Modern and Ancient Geosynclinal Sedimentation, SEPM special publication, SEPM Society for Sedimentary Geology, 19.

Kerans, C., & Ruppel, S. C. (2020). Composite and high frequency cyclicity in middle Permian shelf carbonates: the San Andres and Grayburg (Guadalupian) succession in the Permian Basin, in Ruppel, S. C., ed., Anatomy of a Paleozoic basin: the Permian Basin, USA (vol. 2, ch. 23): The University of Texas at Austin, Bureau of Economic Geology Report of Investigations 285. *AAPG Memoir 118*, 349–398.

Kerans, C., T. Playton, R. Phelps, & Scott, S. Z.(2013). Ramp to rimmed shelf transition in the Guadalupian (Permian) ofthe Guadalupe Mountains: Deposits, architecture, and controls of carbonate margin, slope, and basinal settings, in K. Verwer, T. E. Playton, and P. M. Harris, eds., Deposits, architecture and controls of carbonate margin, slope and basinal settings: Tulsa, Oklahoma. *SEPM Special Publication 105*, 26–49.

King, P. B. (1942). Permian of west Texas and southeastern New Mexico. *AAPG Bulletin, 26*(4), 535–763. https://doi.org/10.1306/3D933466-16B1-11D7-8645000102C1865D

Koson, S., Chenrai, P. & Choowong, M. (2014). Seismic Attributes and Their Applications in Seismic Geomorphology. *Bulletin of Earth Sciences of Thailand*. Retrieved from shorturl.at/gjsK0, 6, 1–9.

Kvale, E. P., Bowie, C. M., Flenthrope, C., Mace, C., Parrish, J. M., Price, B., Anderson, S., & DiMichele, W. A. (2020). Facies variability within a mixed carbonate-siliciclastic sea-floor fan (upper Wolfcamp Formation, Permian, Delaware Basin, New Mexico). *AAPG Bulletin, 104*(3), 525–563. https://doi.org/10.1306/06121917225

La Marca-Molina, K., Silver, C., Bedle, H., and Slatt, R. (2019). Seismic facies identification in a deepwater channel complex applying seismic attributes and unsupervised machine learning techniques. A case study in the Tarinaki Basin, New Zealand. *SEG*

International Exposition and Annual Meeting, 2059–2063. https://doi.org/10.1190/segam2019-3216705.1.

Lee, B., Khoudaiberdiev, R., Lujan, B., & Verma, S. (2018). Depositional Environment and Sedimentary structures of the Grayburg formation, Midland.

Lewis, A., Karr, B., Bianco, R., & Pollock, S. (2021). Illuminating Fine Scale Geology and Creating Robust Seismic Attributes Using High Trace Density Seismic Data in the Midland Basin. *Unconventional Resources Technology Conference (URTeC) 2021*. https://doi.org/10.15530/urtec-2021-5186

Lindsay, R. F. (2016). Outcrop examples of conventional and unconventional stratigraphic traps in the Permian Basin. Midland. West Texas Geological Society Annual Field Trip. #16-133.

Saller, A.H., & Stueber, A.M. (2018). Evolution of formation waters in the Permian Basin, USA: Late Permian evaporated seawater to Neogene meteoric water. *AAPG Bulletin, 102*, 401-428. http://dx.doi.org/10.1306/0504171612517157

Sarnthein, M. & Koopmann, B.(1980). Late Quaternary deep-sea record of northwest African dust supply and wind circulation. *Palaeoecology of Africa, 12*, 239-253

Marfurt, K. J., & Alves, T. M. (2015). Pitfalls and limitations in seismic attribute interpretation of tectonic features. *Interpretation, 3*(1), SB5–SB15. https://doi.org/10.1190/INT-2014-0122.1

Maurya, S. P., & Sarkar, P. (2016). Comparison of Post stack Seismic Inversion Methods: A case study from Blackfoot Field, Canada. *International Journal of Scientific & Engineering Research, 7*(8), 1091–1101.

Matchus, E.J., & Jones, T.S. (1984). East-west cross section through Permian Basin of West Texas. *West Texas Geological Society Publication*, 84-79.

Mayall, M., Jones, E., & Casey, M. (2006). Turbidite channel reservoirs-Key elements in facies prediction and effective development. *Marine and Petroleum Geology*, *23*(8), 821–841. https://doi.org/10.1016/j.marpetgeo.2006.08.001

McHargue, T., Pyrcz, M. J., Sullivan, M. D., Clark, J. D., Fildani, A., Romans, B. W., Covault, J. A., Levy, M., Posamentier, H. W., & Drinkwater, N. J. (2011). Architecture of turbidite channel systems on the continental slope: Patterns and predictions. *Marine and Petroleum Geology*, *28*(3), 728–743. https://doi.org/10.1016/j.marpetgeo.2010.07.008

Meissner, F. G. (1972). Cyclic sedimentation in middle Permian strata of the Permian Basin, in Elam, J. G., and Chuber, S., eds., Cyclic sedimentation in the Permian Basin. West Texas Geological Society, 203–232.

Mitchum, R.M., & Van Wagoner, J.C. (1991). High frequency sequences and their stacking patterns: sequence stratigraphic correlation evidence of high frequency eustatic cycles. *Sedimentary Geology, 70*, 131–160. https://doi.org/10.1016/0037-0738(91)90139-5

Mitchum, R.M., Vail, P.R. & Thompson, S. (1977). Seismic stratigraphy and global changes of sea level, Part 2: The depositional sequence as a basic unit for stratigraphic analysis. *AAPG Memoir, 26*, 53-62. https://doi.org/10.1306/M26490C4

Moscardelli, L., Ochoa, J., Hunt, I. & Zahm, L. (2019). Mixed siliciclastic–carbonate systems and their impact for the development of deep-water turbidites in continental margins: A case study from the Late Jurassic to Early Cretaceous Shelburne subbasin in offshore

Nova Scotia. *AAPG Bulletin, 103*, 2487–2520. https://doi.org/10.1306/02151917318.

Mueller, J.E. (1968). An introduction to the hydraulic and topographic sinuosity indexes. *Annals of the American Association of Geographers, 58* (2), 371–385. https://doi.org/10.1111/j.1467-8306.1968.tb00650.x

Murat Alyaz, A. (2022). Interpretational variations of seismic attribute analysis as compared within the time and depth domains. University of Oklahoma.

Nance, H. S. (2006). Middle Permian Basinal Siliciclastic Deposition in the Delaware Basin: the Delaware Mountain Group (Guadalupian).

Niyazi, Y., Eruteya, O. E., Omosanya, K. O., Harishidayat, D., Johansen, S. E., & Waldmann, N. (2018). Seismic geomorphology of submarine channel-belt complexes in the Pliocene of the Levant Basin, offshore central Israel. *Marine Geology*, *403*(April), 123–138. https://doi.org/10.1016/j.margeo.2018.05.007

Petersen, L. M., & Jacobs, R. S. (2003). Stratigraphic and lithologic zonation in the East Cowden Grayburg Unit, Ector County, Texas: Potential for horizontal re- development of a mature waterflood? (abs.). *AAPG Southwest Section Meeting*. http://www .searchanddiscovery.com/abstracts/html/2003/sw/petersen .htm

Peterson, F. (1988). Pennsylvanian to Jurassic eolian transportation systems in the Western United States, in Kocurek, Gary, ed., Late Paleozoic and Mesozoic eolian deposits of the Western Interior of the United States. *Sedimentary Geology, 56*(1), 4, 207–260. https://doi.org/10.1016/0037-0738(88)90055-3

Peyton, L., Bottjer, R., & Partyka, G. (1998). Interpretation of incised valleys using new 3-D seismic techniques: A case history using spectral decomposition and coherency. *The*

Leading Edge, *17*, 1294-1298. https://doi.org/10.1190/1.1438127

Phelps, R. M., & Kerans, C. (2007). Architectural characterization and three-dimensional modeling of a carbonate channel-levee complex: Permian San Andres Formation, Last Chance Canyon, New Mexico, U.S.A. *Journal of Sedimentary Research, 77*(11–12), 939–964. https://doi.org/10.2110/jsr.2007.085

Pranter, M. J., Hurley, N. F., & Davis, T. L. (2004). Anhydrite distribution within a shelf-margin carbonate reservoir: San Andres Formation, Vacuum Field, New Mexico, USA. *Petroleum Geoscience, 10,* 43–52. https://doi.org/10.1144/1354-079302-547

Ray, A., Khoudaiberdiev, R., Bennett, C., Bhatnagar, P., Boruah, A., Dandapani, R., Maiti, S., & Verma, S. (2022). Attribute-assisted interpretation of deltaic channel system using enhanced 3D seismic data, offshore Nova Scotia. *Journal of Natural Gas Science and Engineering, 99*, ISSN 1875-5100. https://doi.org/10.1016/j.jngse.2022.104428.

Robinson, K. (1988). Petroleum Geology and Hydrocarbon Plays of the Permian Basin Petroleum Province, West Texas and Southeast New Mexico. *U.S. Geological Survey Open-File Report 1988-450Z.*

Oriel, S. & Myers, D. (1967). Crosby West Texas Permian basin region, Chapter CE.D. McKee, S.S. Oriel (Eds.), Paleotectonic Investigations of the Permian System in the United States. *U.S. Geological Survey Professional Paper P 0515*, 17-60.

Sacrey, D. & Roden, R. (2014). Understanding Attributes and Their Use in the Application of Neural Analysis – Case Histories Both Conventional and Unconventional. American Association of Petroleum Geologists. *Geoscience Technology Workshop, Permian and Midland Basin New Technologies*.

Sanchez, D., Santana, T., & Brinkworth, W. (2018). Geomorfología sísmica mediante Descomposición Espectral para el Entendimiento del Modelo Geológico del Grupo Cuyo en la Cuenca Neuquina. *10o Congreso de Exploración y Desarrollo de Hidrocarburos*.

Santana, T., & Elizondo, M. E. (2019). Frequency Decomposition to reveal and validate geological concepts for further development. Examples from Cerro Piedra area, western San Jorge basin, Frequency Decomposition to Reveal and Validate Geological Concepts for Further Development Examples. *2019 International Conference and Exhibition*. https://doi.org/10.1306/11279Santana2019

Sarnthein M., & Diester-Haass, L. (1977). Eolian-sand turbidites. *J Sed Petr, 47*, 868–890.

Silver, B.A. & Todd, R.G. (1969). Permian Cyclic Strata, Northern Midland and Delaware Basins, West Texas and Southeastern New Mexico. *AAPG Bulletin, 53*, 2223-2251. https://doi.org/10.1306/5D25C94D-16C1-11D7-8645000102C1865D

Sonnenfeld, M. D., & Cross, T. A. (1993). Volumetric partitioning and facies differentiation within the Permian upper San Andres Formation of Last Chance Canyon, Guadalupe Mountains, New Mexico; in Loucks, R. G. and Sarg, J. F., eds., Recent advances and applications of carbonate sequence stratigraphy. *American Association of Petroleum Geologists Memoir*.

Todd, R.G. (1976). Oolite-bar progradation, San Andres Formation, Midland Basin, Texas. *AAPG Bulletin, 60*, 907-925. https://doi.org/10.1306/C1EA35DC-16C9-11D7-8645000102C1865D

Turnini, A. (2015). Stratigraphic And Structural Controls on Mississippian Limestone and

Tripolitic Chert Reservoir Distribution Using Seismic-Constrained Reservoir Characterization and Modeling, Northern Oklahoma. University of Oklahoma. http://eprints.ums.ac.id/37501/6/BAB II.pdf

Van Siclen, D. C. (1958). Depositional topography--examples and theory. *AAPG Bulletin, 42*(8), 1897-1913. https://doi.org/10.1306/0BDA5B88-16BD-11D7-8645000102C1865D

Veeken, P. C. H., & Da Silva, M. (2004). Seismic inversion methods and some of their constraints. *First Break, 22,* 47-70, https://www.researchgate.net/publication/277392423_Seismic_Inversion_Methods_and_some_of_their_constraints

Verma, S., & Scipione, M. (2020). The early Paleozoic structures and its influence on the Permian strata, Midland Basin: Insights from multi-attribute seismic analysis. *Journal of Natural Gas Science and Engineering, 82*(August), 103521. https://doi.org/10.1016/j.jngse.2020.103521

Verma, S., Chopra, S., Ha, T., & Li, F. (2022). A review of some amplitude-based seismic geometric attributes and their applications. *Interpretation, 10*(1), B1–B12. https://doi.org/10.1190/INT-2021-0136.1

Verma, S., Yalcin, E., Ortiz-Sanguino, L., Yandell, J., Henderson, M., & Trentham, R. (2023) Seismic attribute and well log analysis for channel characterization in the Upper San Andres and Grayburg Formations of the Midland Basin, Texas. *Energy Geoscience*. *ENGEOS_100188, in press.*

Ward, R., & Trentham, R. (2020). Personal communication; discussion notes by Trentham based on a series of discussions between Ward and Trentham.

Wilson, T., Handke, M., Loughry, D., Waite, L., & Lowe, B. (2019). Regional geologic characterization of the Grayburg-San Andres reservoir for saltwater disposal management, Midland Basin, TX. *Unconventional Resources Technology Conference 2020 (URTeC 2020)*, 1–12. https://doi.org/10.15530/urtec-2019-902

Yandell, J., Whaley, C., Verma, S., & Henderson, M. A. (2019). Integration of 3D seismic, well, and core data to investigate channel-like features in the Grayburg Formation, Midland Basin. *AAPG SWS Section Annual Meeting*.

Yalcin, E., Yandell, J., & Verma, S. (2019). Study of channel like features in Grayburg Formation of Midland Basin. *University of Texas at the Permian Basin Poster Competition*.

Zhai, R. & Pigott, J. (2021). High-resolution sequence stratigraphy and multiple attributes analysis of the Bone Spring turbidite system, northern Delaware Basin. *SEG/AAPG/SEPM First International Meeting for Applied Geoscience & Energy 2021*. https://doi.org/10.1190/segam2021-3594951.1

Zhang, B., Lin, T., Guo, S., Davogustto, O., & Marfurt, K.J. (2016). Noise suppression of time-migrated gathers using prestack structure-oriented filtering. *Interpretation, 4*, SG19-SG29. https://doi.org/10.1190/INT-2015-0146.1

Zhao, T., Zhang, J., Li, F. & Marfurt, K.J. (2016). Characterizing a turbidite system in Canterbury Basin, New Zealand, using seismic attributes and distance-preserving self-organizing maps. *Interpretation*, *4*, SB79–SB89, https://doi.org/10.1190/INT-2015-0094.1.

Appendices

Appendix A. Table with details of the seismic acquisition.

Further detail can be found in Lewis et al. (2021).

Seismic Survey Acquisition Parameters		
Vintage	2019	2009
CDP Bin Dimensions	41.25´x41.25´	110´x110´
Nominal Fold	1024	70
Record Length	6 s	3 s
Source interval	82.5´ (dual source lines)	220´
Sources per Square Mile	1370	96
Source Line Spacing	495'	1320'
Number of Vibrators	2	3
Sweeps per Vibrator Point	1	3
Sweep Bandwidth	2-92 Hz	6-96 Hz
Sweep Length	24 s	8 s
Linear or nonlinear sweep	Non-linear/Custom Sweep	Linear
Receiver Interval	165'	220'
Receiver Line Spacing	495'	1320'
Receivers per Square Mile	342	96
Recording Geometry	64x192=12288	14x120=1680
Recording Swath Dimensions	15840'x15840'	7920'x13200'
Off-Diagonal (Max. Offset)	22401'	15394'
Trace Density Per Square Mile	16777216	161280

Appendix B. Total porosity and well-log impedance cross-plots workflow to differentiate between rock types.

(a) Total porosity and well-log p-impedance cross-plot of all zones color-coded by facies. Note similarity in acoustic impedance ranges and porosity as well. b) Total porosity and well-log p-impedance cross-plot of all zones color-coded by facies with my alternative solution to discriminate among facies using the PHIT vs AI plot. Users can dynamically draw polygons that best represent facies in the P-impedance inverted volume based on the at-well-location plot.

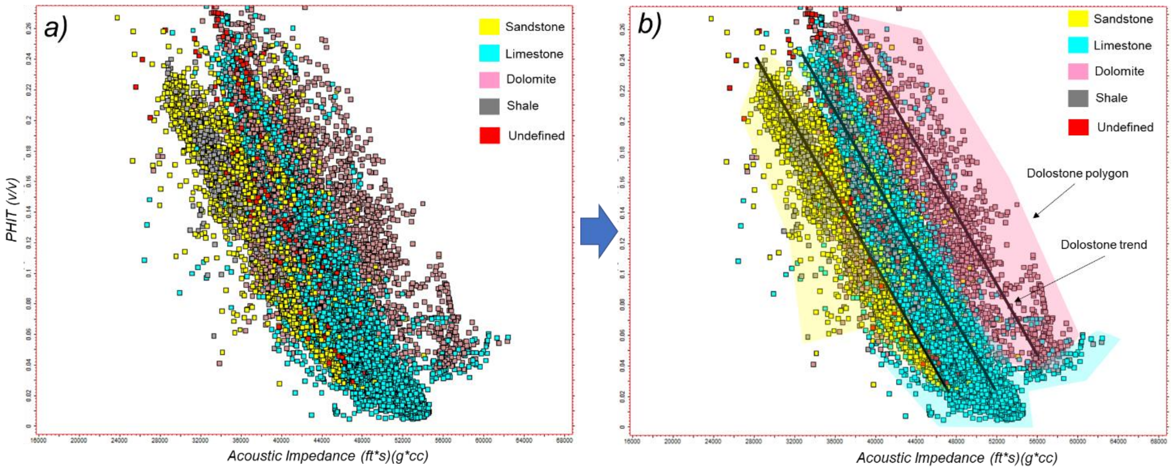

Appendix C. Inversion analysis vs number of iterations.

Note that after 5 iterations P-impedance error increases.

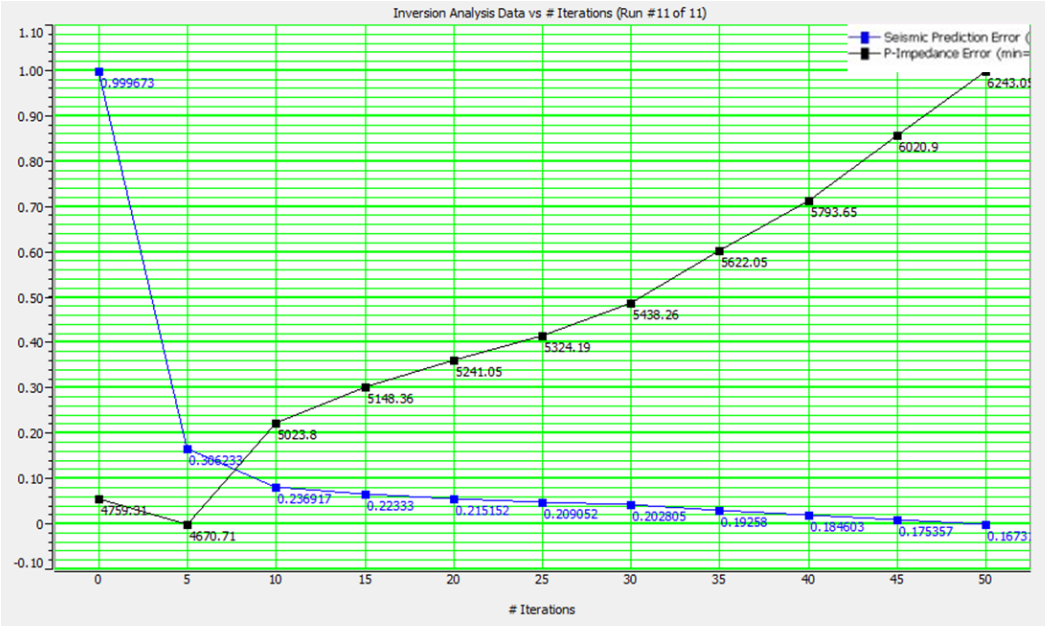

Appendix D. histogram of the Upscaled rock-type logs and original rock types.

Notice that the model grid (green bars) captures the vertical variability of the original well logs.

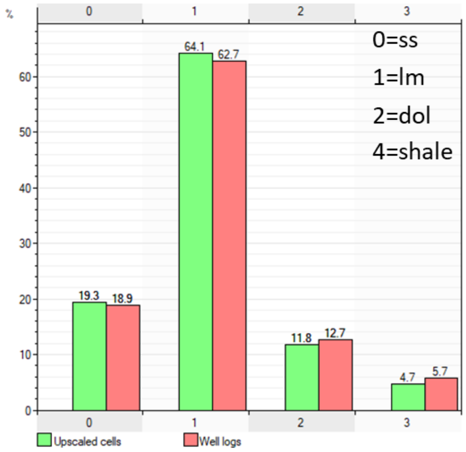

Appendix E. Vertical proportion curve

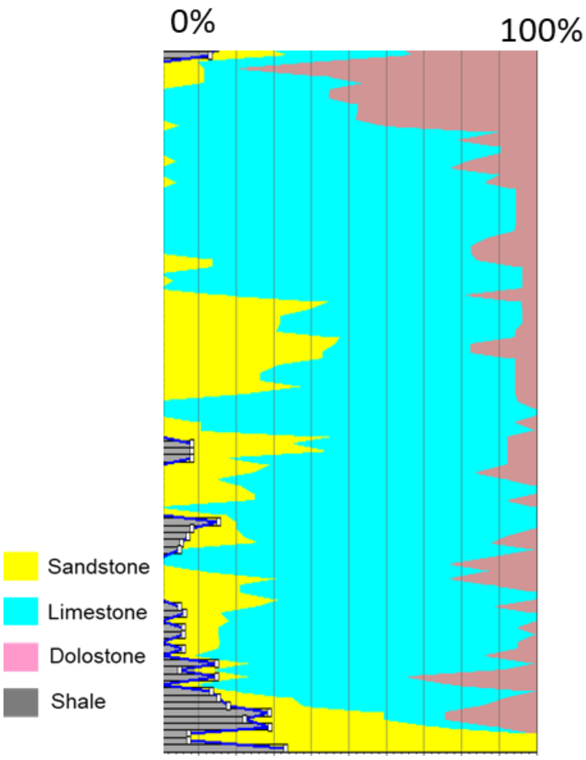

Appendix F. Variogram tables for dolostone and limestone rock types.

Azimuth was set to zero for all of the zones.

Variogram parameters for lithology modeling (Dolostone)			
Zone	Major	Minor	Vertical
A	20000	20000	50
B	20000	20000	100
C	200000	20000	100
D	20000	20000	120
E	20000	20000	70
F	20000	20000	80
G	20000	20000	100
H	20000	20000	80
I	20000	20000	100

Variogram parameters for lithology modeling (Limestone)			
Zone	Major	Minor	Vertical
A	20000	20000	60
B	20000	20000	100
C	200000	20000	100
D	20000	20000	80
E	20000	20000	80
F	20000	20000	80

G	20000	20000	100
H	20000	20000	90
I	20000	20000	100

Appendix G. Illustration of the geomorphological parameters presented in Table 2. Modified from Niyazi et al. (2018).

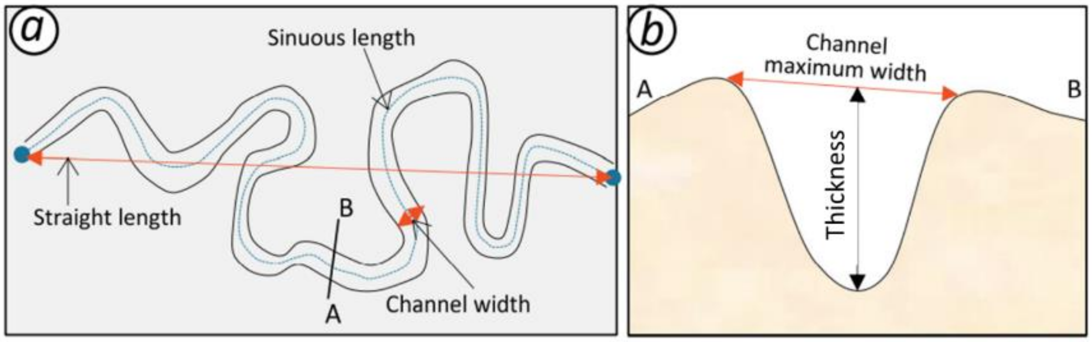

Appendix H. Inversion results and qualitative QC.

a) The results of the inversion at the well scale using as example the well 9. Note that the interval in yellow corresponds to the inversion interval (top LSA to top Queen). The first track shows P impedance computed from the well logs (blue) and the inversion p-impedance (red). Second track shows the correlation of about 97, third track is extracted seismic wiggles and fourth track is the error between the computed AI in the well logs and the inversion result. b) Same layout as a) but for well 1, which showed the highest error of the three wells used as input for the inversion (~38%). c) P-impedance qualitative comparison between the inversion result (background) and the AI at the well log (overlain) in an inline section of wells 9 and 10. d) Same as c) but for well 1 evidence the poor match in the deeper portion of the inversion.

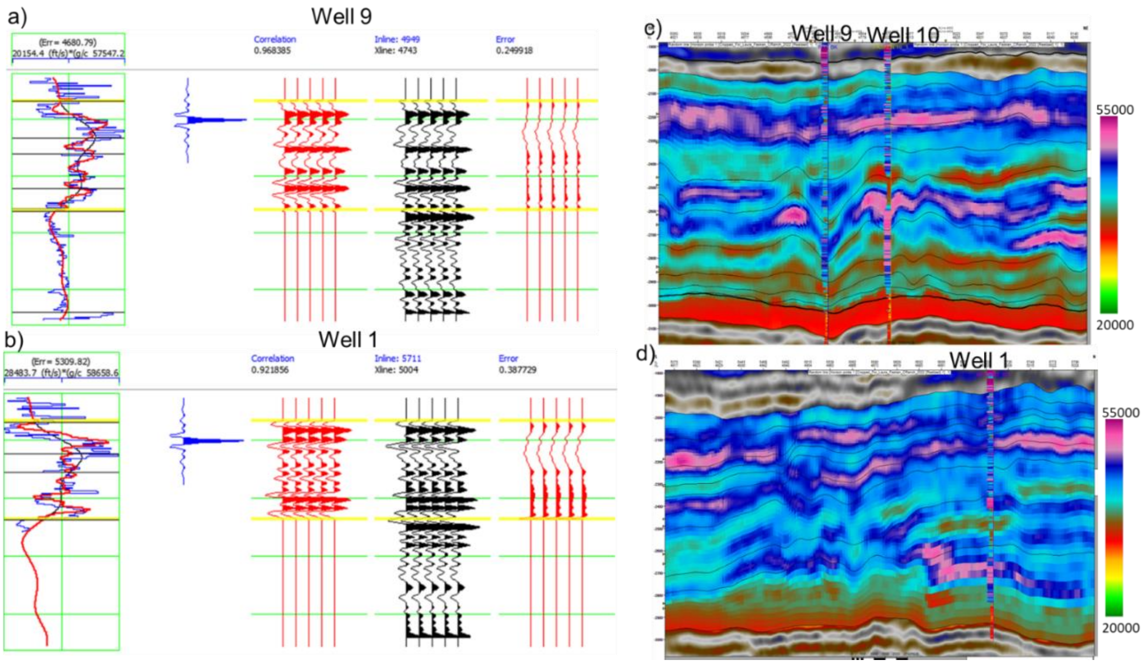
a)
Well 9
(Err= 4680.79)
20154.4 (ft/s)*(g/c 57547.2
Correlation
0.968385
Inline: 4949
Xline: 4743
Error
0.249918
b)
Well 1
(Err= 5309.82)
28483.7 (ft/s)*(g/c 58658.6
Correlation
0.921856
Inline: 5711
Xline: 5004
Error
0.387729
c)
Well 9
Well 10
55000
20000
d)
Well 1
55000
20000

Appendix I. Probability maps of limestone for each zone.

Warm colors indicate higher proportions of limestone. Note the progradation from zone H to zone D.

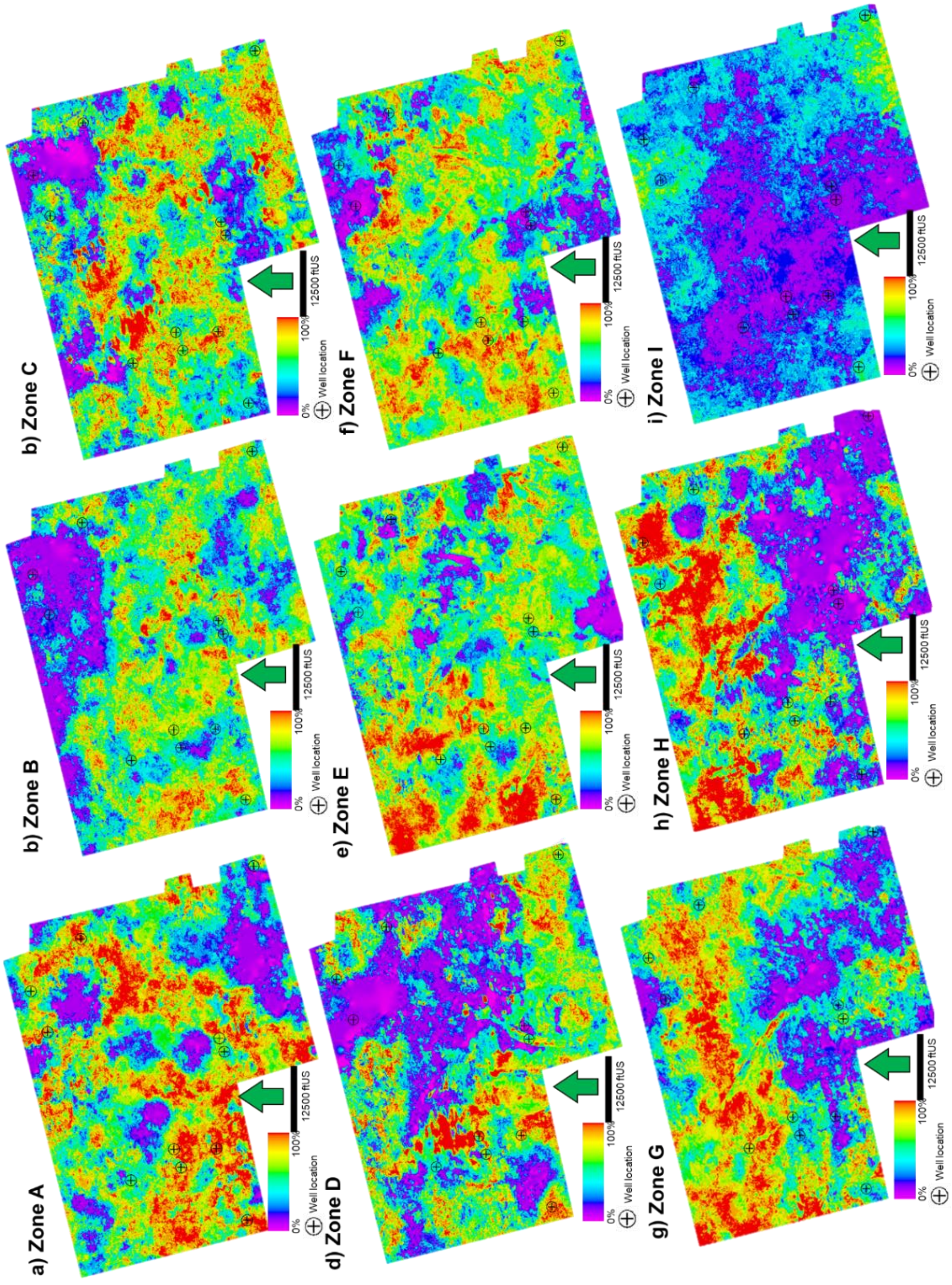

Appendix J. Probability maps of dolostone for each zone.

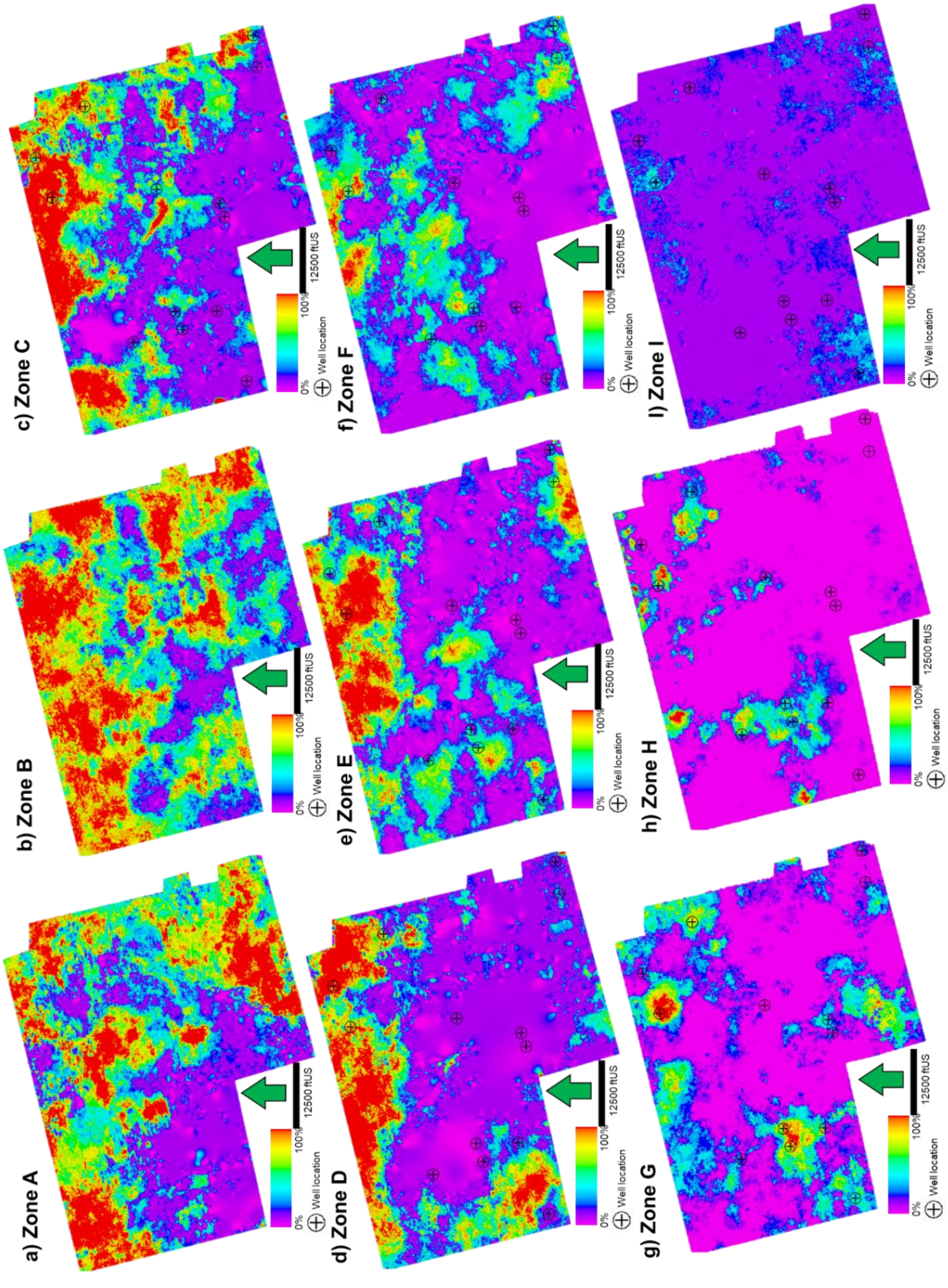

Appendix K. Self-organizing maps (SOM) and generative topographic maps (GTM) workflow for facies identification.

Multiple self-organizing maps and generative topographic maps were generated to facilitate the geobody generation. This methodology was NOT included into the main thesis but could help future projects. These techniques were hypothesized to provide clusters that will isolate the siliciclastic facies, mostly restricted to the channel fills. Attributes selected were the ones that by individual inspection seem to show a correlation to the channel facies: positive amplitude curvature, coherent energy, relative acoustic impedance, frequency CWT 37, Peak Magnitude, Peak Frequency. Different combinations were selected, while parameters kept the same: 256 classes, 5 data training iterations, etc. Initially, the SOMs were run in for the complete seismic volume within 800-1200 milliseconds, but to improve the results, I cropped the volume to the south portion (modeling area) as well as vertically (900-1100 ms) to enhance the classification. However, in both instances the classification provided very similar results and channel fills/siliciclastic were not picked by a single/multiple neurons that could be distinctive enough from the rest of the seismic facies. To prove the correlation between the siliciclastic facies and the neurons, I extracted the SOM over the wells and compare if the locations shown a trend. Unfortunately, the neurons/machine learning results were not conclusively related to sandstones/siliciclastics. An explanation for this is that the resolution of the seismic, even though it resolves some of the sands, thin sandstone accumulation specially moving towards the shelf (north side wells). Alternatively, the seismic attributes selected in combination could not been appropriate or that unlike the hypothesis states where all the channel incisions are filled with sands (i.e., it could be a combination of other minerals that make it undetectable to the sandstone ρmaa-Umaa analysis).

To prove that the algorithm (SOM) was not the limitation on the resolution of this problem, I ran generative topographic maps (GTM), using attribute combination similar to SOM1, obtaining very similar results.

SOM's complete volume-800 to 1200 ms				
Attribute	**SOM 1**	**SOM2**	**SOM 3**	**SOM 4**
ePos	🟩	🟩		🟩
Coherent Energy	🟩	🟩		🟩
Relative Acoustic Impedance	🟩	🟩		🟩
Sweetness				
Freq. Comp. 37	🟩	🟩	🟩	🟩
Freq. Comp. 42			🟩	
Peak Magnitude		🟩	🟩	🟩
Peak Frequency			🟩	
Apparent Dip				🟩

SOM's complete volume-900 to 1100 ms				
Attribute	**SOM 5**	**SOM 6**	**SOM 7**	**GTM**
ePos	🟩			
Coherent Energy	🟩	🟩	🟩	🟩
Relative Acoustic Impedance	🟩	🟩	🟩	🟩
Sweetness			🟩	🟩
Freq. Comp. 37	🟩	🟩	🟩	🟩
Freq. Comp. 42				
Peak Magnitude		🟩	🟩	🟩
Peak Frequency				🟩

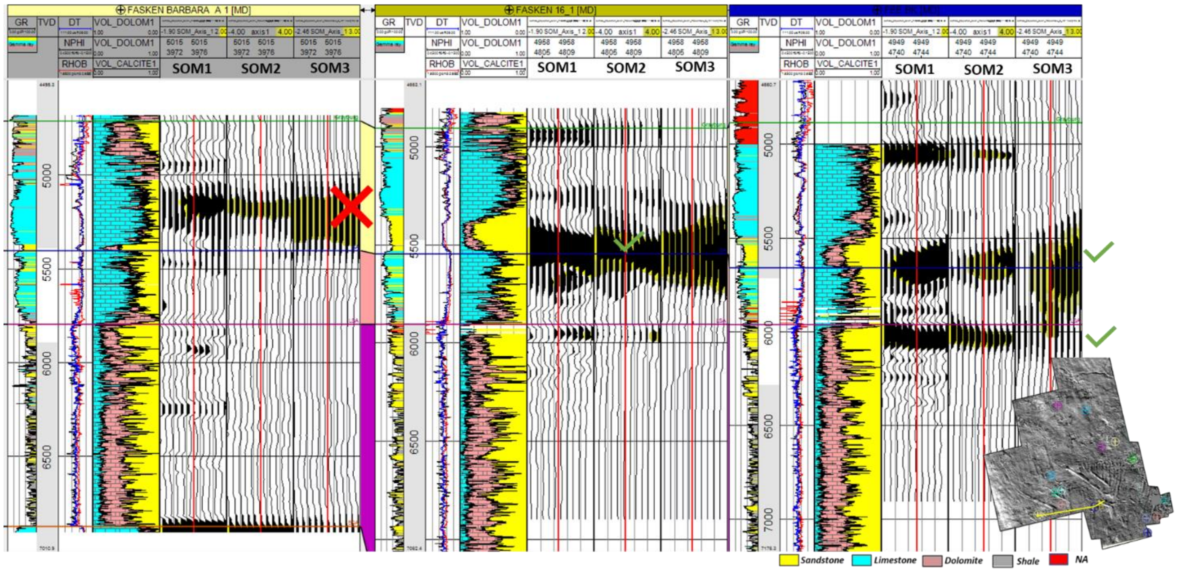

This well penetrates a channel!